Facilitating Dielectric Elastomer Actuator Multilayer Fabrication and Performance Through Low-Contact-Resistance Hybrid Electrodes, Scalable Vacuum Filtration, and Adaptive Pre-Clearing

Andy J. Cohen, Michelle C. Yuen, Mady N. Corrigan, Siyi Xu, Robert J. Wood

Abstract

Networks of conductive nanoparticles have been used as electrodes for dielectric elastomer actuator multilayers because of their excellent extensibility and low added stiffness. Nanoparticle network topography, however, has typically effected a tradeoff between conductivity and breakdown strength. This has limited actuators to a corresponding tradeoff between either high operating frequencies and efficiencies or high stresses, strains, and energy densities. We resolve this tradeoff by spatially patterning multiple nanoparticles to produce hybrid electrodes. Sparse networks of high-aspect-ratio carbon nanotubes allow for self-clearing in the body of the electrode, yielding 54.7 V/µm breakdown strength, 86.4% that of the neat elastomer. Dense networks of low-aspect-ratio carbon black at the external interfaces, meanwhile, provide low contact resistance (44.09 kΩmm). We also develop two tools essential for their practical deployment: a scalable fabrication process and an automated pre-clearing algorithm. The fabrication method leverages our batch spray and stamp paradigm in concert with vacuum filtration to scalably deposit nanoparticle electrodes with minimal parameter tuning, enabling the production of a 100-layer actuator capable of 14% strain. The adaptive pre-clearing algorithm discriminates between and responds to a range of defect-induced failures in newly fabricated actuators, eliminating the need for human oversight and standardizing the break-in procedure.

1 Introduction

Dielectric elastomer actuators (DEAs) are a promising artificial muscle technology: they are strong enough to lift 50× their own weight [1], fast enough to operate at tens of thousands of Hz [2], and soft enough to withstand shocks and impacts that would destroy other actuators [3]. Their direct electromechanical transduction mode also allows easy integration with electronics – when a voltage is applied to electrodes sandwiching a thin elastomer membrane, a Maxwell stress compresses the membrane through its thickness and expands it in-plane.

While the energy density of a DEA membrane can match and even exceed that of natural muscle (0.4-40 J/kg) [1, 4], the total energy output of a single-layer device is limited. In order to produce an electric field high enough for actuation (∼10-100 V/µm) at the voltages that lab-scale amplifiers can supply (∼1-10 kV), the membrane must be ∼10-100 µm thick. This low thickness limits the total device volume and thus its energy output. To scale up thickness - and thus energy output - alternating layers of electrodes and elastomer membranes are often stacked to create a dielectric elastomer actuator multilayer (DEAM) [5–7].

The electrodes in a DEAM must meet strict electromechanical requirements. The elastomers have a low elastic modulus, typically tens to hundreds of kPa, to maximize actuator strain (typically 10-30% [8]). To avoid limiting this strain, the electrode layer must add negligible mechanical impedance. The electrodes must also exhibit low electrical impedance to avoid limiting operating frequency (i.e., considering the low-pass behavior of the equivalent electrical circuit), and must remain conductive at the maximum operating strains. Finally, in order to maximize the applied electrical field and thus mechanical work output, the electrodes must not excessively degrade the breakdown strength of the device.

These requirements are typically met using networks of conductive nanoparticles (NPs) such as carbon black (CB) or carbon nanotubes (CNTs) [4, 8–11]. These NP networks provide lower stiffness and higher maximum stretches than solid metal or polymer films, and present fewer practical implementation challenges than liquid metals, carbon grease, and ionogels [8]; they are relatively easy to pattern, as they can be mixed into inks and deposited wet or can be stuck onto elastomers in a dry stamping process, and they adhere to the elastomer surface rather than migrating along or into it. The particles can be deposited in nanometer-thick layers in which particles and their aggregates can slide past each other while maintaining contact, retaining conductivity even when stretched [8]. Percolative NP networks also achieve low sheet resistances (< 100 kΩ/□) at low areal concentrations of particles, allowing for minimal stiffening ($< 10\%$ of elastomer stiffness) [12].

While NP networks meet the stated electromechanical requirements, it is difficult to design a single NP ink that simultaneously maximizes all the performance variables of DEAMs and encapsulated DEAs. One particular challenge is

the tradeoff between breakdown strength and conductivity, quantities which are needed for high-stress and high-frequency operation, respectively.

Dielectric breakdown occurs when the electric field applied across the elastomer dielectric exceeds the local breakdown strength and the typically-insulating dielectric permits an arc of current. This current, often on the order of 1 mA [1, 13–16] can permanently damage and short-circuit the dielectric, causing a catastrophic failure of the whole actuator. These highly-stochastic events are often nucleated by manufacturing defects such as air bubbles, thickness variations, and nanoparticle protrusions into the elastomer layer [8,15]. These are infeasible to entirely prevent, so DEAM designers have increasingly employed fault-tolerant electrodes based on "self-clearing" networks of NPs. These self-clearing networks comprise high-aspect-ratio particles, typically CNTs, which can each tolerate relatively low currents ($\sim$20 μA) before being destroyed [17]. When current spikes above this limit during a breakdown event, it destroys a patch of CNTs surrounding the failure site, rendering the area non-conductive and preventing further current flow to the site (Fig. 4B). This self-clearing effect prevents catastrophic global failure of the actuator. Compared to non-clearing NP networks composed of low-aspect-ratio NPs (e.g., CB particles), self-clearing networks enable both higher and more consistent effective breakdown strengths [13, 18].

CNT-based electrodes are typically "pre-cleared" after fabrication to ensure reliable operation. A series of increasing voltages is applied to the device; at each voltage, breakdown events occur, clearing away defects that would otherwise be encountered during operation. Once the device has been cleared to the desired operational voltage, it can be safely and reliably operated up to that voltage; pre-cleared DEAMs with CNT electrodes have been operated for millions of actuation cycles [13, 16]. This process is essential for maximizing the operating voltage of self-clearing electrodes [8, 13], but the methods by which it is performed have been manual, uncontrolled, and unable to adapt their settings to clear the wide range of defects encountered. Most pre-clearing is performed by manually applying stepped DC signals and then waiting until pre-clearing events have ceased with little to no real-time feedback or control of the process [1, 16, 19]. This can cause excessive degradation; attempting too rapid of a voltage increase at can allow many clearing events to occur simultaneously, resulting in excessive degradation [13]. Despite this, previous work has generally applied clearing voltages in large steps of tens to hundreds of volts [1, 15, 16]. Previous pre-clearing procedures have also typically permitted large clearing currents ($>$ 100 µA) for relatively long durations ($>$ 1 s) [1, 16, 18]. Previous work has shown, though, that longer pre-clearing durations can lower breakdown strength [13]. One second is enough time for many breakdown events to occur; as shown in Movie S1, breakdown events can occur on the timescale of ms. Additionally, existing pre-clearing process do not account for the variability in clearing behavior resulting from heterogeneous defects. Each defect can fail at a different voltage, with a different current, and with one of two failure modes: while most defects self-clear after a short spike in current, some form durable short circuits that cannot be cleared, requiring the device to be discarded [4,15]. Finally, previous protocols required minutes to hours of human operation and/or oversight, a labor requirement that precludes industrial-scale pre-clearing and thus commercial deployment of DEAs.

In addition to their pre-clearing requirements, self-clearing CNT networks suffer from increased contact resistance in exchange for increased breakdown strength. In DEAMs and encapsulated DEAs, the dielectric completely encapsulates and electrically isolates the electrodes from external driving electronics. In order to create an external electrical interface (EEI), a cross-sectional cut is made through the elastomer and electrode layers at the contacts of the DEAM and a conductive ink is applied, as shown in Figs. S12 and S13. Sparsely-distributed CNTs with diameters on the order of 1 nm provide little exposed surface to connect to at this cross sectional interface, yielding high contact resistances that can dominate total device resistance [16, 20] and limit device operating frequency and efficiency. While more CNTs can be added to improve contact resistance at the EEI, breakdown strength is negatively correlated with the areal density of CNTs in the network – as more CNTs are added beyond the percolation threshold, more energy is required to destroy a patch of the network, and clearing becomes less effective [1, 13–15]. Similarly, low-aspect-ratio particles such as CB could be used to provide more cross-sectional area at the EEI, but this would forfeit the ability to self-clear in the body of the electrode. DEAM designers have evaded this issue by adding long contacts that span much of the device's perimeter. However, this adds complexity to subsequent assembly steps and requires designers to accommodate the limits of these designs. In "roll actuators", for example, a stack of high-aspect-ratio rectangular layers is rolled along its long axis to produce a cylindrical actuator that expands longitudinally when actuated [15]. The entirety of each long edge of the precursor rectangle is used as the contact region, and once rolled up, these are electrically and mechanically connected to end caps. Accurately rolling, cutting, painting, and affixing the contacts such that they are both electrically well-connected and mechanically well-affixed requires significant labor. Additionally, the entire length of the long contact must be constrained to a rigid interface, restricting device displacement along the contact length and thus limiting actuation modes [15].

A single nanoparticle ink patterned uniformly over the electrode is thus unable to achieve both high breakdown strength and low resistance. Previous work has employed an additional sputter-coating step to deposit gold films onto the contact region through which the cross-sectional cut is made [3, 21]. While this enhanced the robustness of the electrical interface, sputter coating adds significant complexity, cost, and time to the manufacturing process [22], and these drawbacks scale with the number of layers in the DEAM (practically limiting them to few layers). The ability to

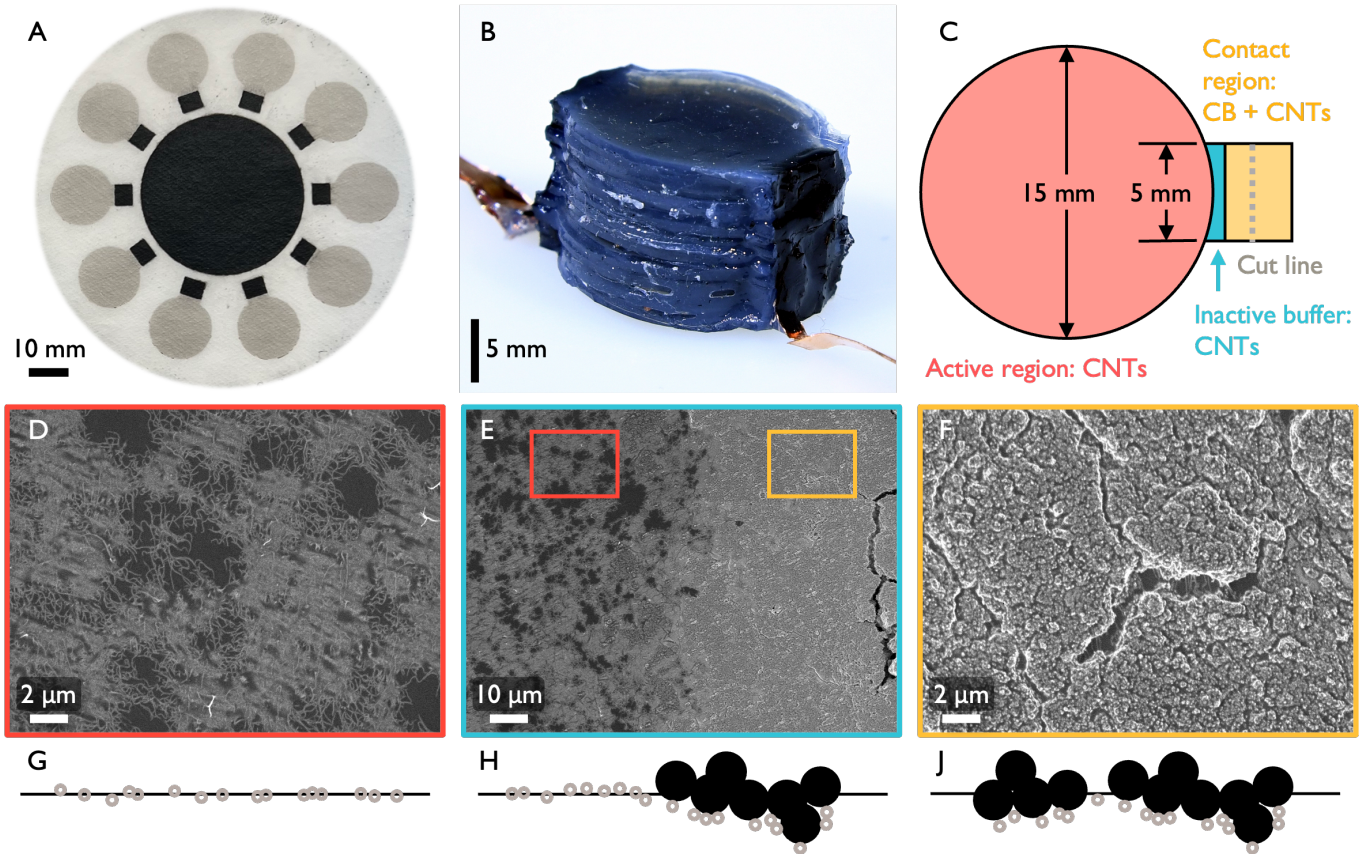

Figure 1: **Architecture of hybrid electrodes** (**A**) Hybrid electrode stamps deposited onto filter paper. A central disk allows for inspection of each batch's sheet resistance. (**B**) A DEAM of 100 active layers made from the stamps in (A). (**C**) Schematic of a single paddle electrode. (**D**) Scanning electron microscope (SEM) image of the active (CNT-only) region of an electrode. (**E**) SEM image of the transition between buffer (CNT-only) and contact (CB+CNT) regions. Zoom boxes are for size reference – they do not represent exact locations of images in (D) and (F). (**F**) SEM image of the contact (CB+CNT) region. A crack in the center shows CNTs beneath the CB. All SEM images were taken after stamping onto the elastomer. (**G**) Graphical representation of the cross section of CNT-only networks seen in (D). The black line represents the interface between elastomer layers, and the gray circles represent the cross-sections of CNTs. (**H**) Representation of the cross section of the transition region in (E). CB particles are represented by black disks. (**J**) Depiction of the CB+CNT region cross-section. The greater contact area of the CB network provides lower contact resistance.

spatially pattern multiple NP inks with a single process would offer a simpler, cheaper, and faster alternative.

In this work, we leverage and refine our previously-described batch-spray and stamp (BSS) electrode fabrication paradigm [12] to pattern "hybrid" electrodes with multiple nanoparticle inks in distinct regions (Figure 1). We demonstrate how hybrids composed of CB contacts and CNT active regions can achieve low contact resistances while maintaining high breakdown strengths, resolving the common breakdown-conductivity tradeoff. Moreover, we present an adaptive algorithm for the essential but ill-standardized process of "pre-clearing" DEAMs after their fabrication. This combination of a hybrid electrode design concept and the methods to fabricate and pre-clear them represents a suite of tools for improving both the performance and practicability of DEAM concepts.

Our BSS electrode fabrication paradigm allows us to selectively pattern multiple NP inks with only minimal tuning of manufacturing and material parameters. Rather than directly depositing NP inks onto the surface of each elastomer layer, BSS processes first spray NP inks onto a separate carrier substrate to form the electrode and then dry-stamp it onto the surface of each elastomer layer. Unlike wet deposition processes such as jetting and gravure printing which must tune oft-conflicting material properties [11, 23] to account for each ink's interactions with the elastomer substrate, BSS processes require only minimal tuning to deposit inks onto a single, separate carrier substrate. We further reduce tuning requirements in this work by employing vacuum filtration to mechanically – rather than evaporatively – separate NPs from their solvents across a porous carrier substrate, which avoids inhomogeneities such as "coffee ring" effects without heavily tuning ink properties such as surface tension [8]. The decoupling of ink manufacturing properties from elastomer

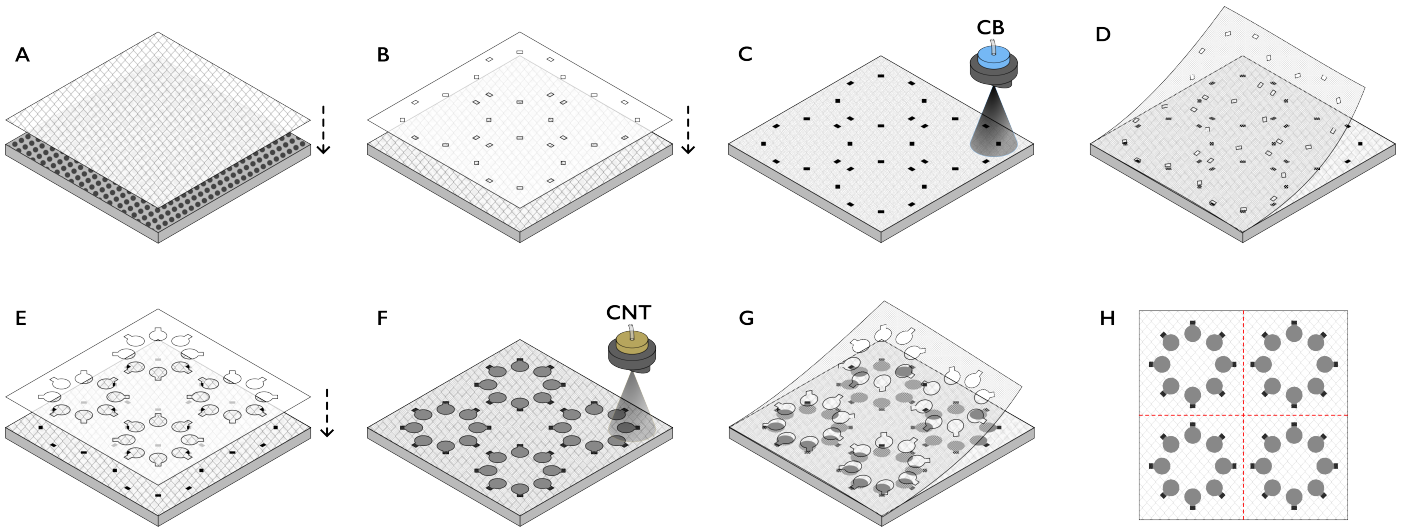

Figure 2: **Hybrid electrode batch spray process.** (**A**) A sheet of filter paper is placed atop the porous aluminum (Metapor BF100 AL, CMT Materials) vacuum plate. (**B**) A laser-cut PET mask defining the CB+CNT contact regions is placed atop the filter paper. (**C**) An atomizing nozzle sprays CB ink through the mask while the vacuum is applied, depositing a network of CB onto the surface of the filter paper in the contact regions. (**D**) The CB mask is removed and discarded. (**E**) A mask defining the CNT regions (both electrode body and contact regions) is applied. (**F**) A CNT ink is sprayed through an atomizing nozzle and filtrated on the surface of the filter paper. (**G**) The CNT mask is removed and discarded. (**H**) The completed hybrid electrode stamp. After the stamp has dried, it is typically partitioned into smaller areas for stamping multiple electrode layers.

substrate properties allows for more rapid development of a library of NP inks with varying performance characteristics, and allows inks to be modularly deposited atop and in combination with one another. By applying a series of masks and spraying through them, these inks can be deposited only where are they advantageous. Additionally, because the electrodes are deposited on separate carrier substrates rather than directly on the surface of each elastomer layer, they can be batch-produced in large sizes and quantities in advance of actuator assembly. The electrode can then be quickly stamped onto each elastomer layer, increasing fabrication process throughput. The advantages of BSS processes are further elaborated in [12].

We exploit the spatial patterning capability to resolve the breakdown-conductivity tradeoff in DEAMs and encapsulated DEAs. CNTs patterned throughout the body of hybrid electrodes enable breakdown strengths of 54.7 V/μm, 61% higher than our previous batch-sprayed CB electrodes [12] and 86.4% of the neat elastomer's breakdown strength (63.4 V/μm) [12]. A network of CB and CNTs patterned at the contacts of these electrodes, meanwhile, produce a 32$\times$ drop in contact resistance compared to CNTs alone, from 284.9 kΩ (1425 kΩmm) to 8.817 kΩ (44.09 kΩmm).

We also define and implement an adaptive pre-clearing algorithm that is capable of evaluating and responding to the various failure modes produced by various defects throughout each device. The algorithm limits current magnitude and duration (20 µA for less than 1 ms), applies only the minimum required clearing voltage for each defect, and uses high-frequency (100 Hz) bursts of current to clear durable shorts that have previously been difficult or impossible to clear. This algorithm also allowed us to completely automate the process, eliminating the need for human supervision and opening a pathway to industrial-scale pre-clearing.

2 Fabrication process and device architecture

We fabricate DEAMs by first batch-spraying nanoparticle inks onto 220$\times$220 mm sheets of filter paper (RS40419, Tisch Scientific) to produce hybrid electrodes (Fig. 2). The inks are deposited in two steps: first, a CB ink is sprayed onto filter paper through a mask to pattern the contact regions (Figs. 2A-D), and a vacuum plate underneath the filter separates the solvent from the NPs. This process is repeated with a CNT ink sprayed through a second mask onto both the contacts and body of the electrode (Figs. 2E-G). CB is deposited first to allow stamp-transfer of CNTs; CB otherwise blocks CNT networks from adhering to the elastomer surface. The resulting stamp (electrodes on filter paper) is illustrated in Fig. 2H and pictured in Fig. 1A. Once the stamps have been allowed to fully dry, they are often subdivided into smaller stamps to yield multiple electrode layers from a single spray (Fig. 2J). Complete recipes and deposition processes are detailed in the Supporting Information (Sections A.7.1-A.7.4).

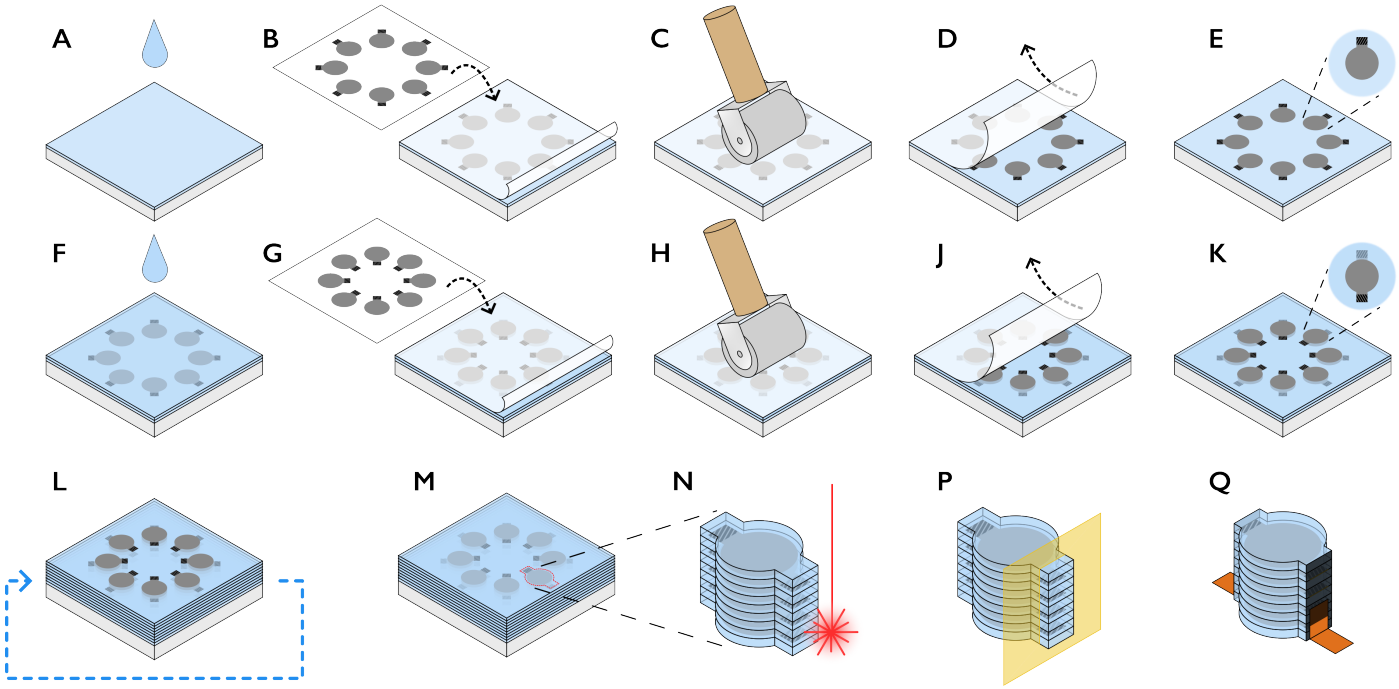

Figure 3: **DEAM assembly and connection process.** (**A**) An elastomer layer is deposited onto an acrylic support substrate – typically via spin-coating – and then cured. The thicknesses of the elastomer layers in the subfigures have been exaggerated for clarity. (**B**) An electrode stamp is applied to the surface of the elastomer. (**C**) A roller is used to apply pressure. (**D**) The carrier substrate (filter paper) is peeled back and discarded. (**E**) The electrode transfers to the elastomer surface. (**F**) Another elastomer layer is deposited and cured atop the electrode. (**G**) Another stamp, this one with contact regions that do not intersect those of the previous stamp, is applied. (**H**) A roller is used to apply pressure. (**J**) The carrier substrate is peeled back and discarded. (**K**) The electrode transfers to the elastomer surface. (**L**) Steps A-K are repeated until a stack with the desired number of layers has been achieved. (**M**) A final encapsulation layer is deposited and cured atop the stack. (**N**) A laser is used to cut out each DEAM from the surrounding elastomer, leaving a thin border of dielectric to avoid short-circuits between layers. (**P**) A knife is used to cut through the contact region and expose cross-sections of the electrode. (**Q**) Colloidal graphite is brushed onto the exposed cross-section to form the external electrical interface to driving electronics, and copper tape or wire is connected to this interface.

The use of vacuum filtration requires less tuning of inks compared to the evaporation process used in [12] because the mechanical separation method depends less strongly on ink and substrate properties such as surface energy. It is also faster – a single spray of a 220×220 mm sheet can be completed in 5 minutes with filtration vs 30 minutes with evaporation. Though vacuum filtration minimizes the tuning requirements of each ink, it has previously been considered unsuitable for scaling and automation [8]. Previous work deposited on relatively small filters (90 mm diameter) by pouring a discrete volume of ink onto the filter and then applying a vacuum underneath [15, 16, 24]. Our process, however, applies a continuous spray of electrode ink while vacuum is applied. The continuity of this method makes it easier to scale and automate (e.g. as a roll-to-roll process). Our use of a low-cost disposable filter substrate also reduces cost by 92% compared to established vacuum filtration and stamp-transfer processes used in [15, 16, 24]. The full cost accounting can be found in Section A.8.

The hybrid electrodes are then stamp-transferred onto an elastomer layer (Fig. 3B-E). Unlike in previous vacuum filtration and stamp-transfer processes wherein a mask is applied to each elastomer layer to pattern the electrode, the electrode pattern has already been fully defined on the stamp during the deposition stage of our process (Fig. 2). This reduces the complexity of and time required for stamping each layer. After stamping, an additional elastomer layer is deposited via spin deposition with a typical thickness of 30-80 µm (Fig. 3F). While this work exclusively uses spin-coated silicone for simplicity of analysis, BSS processes such as that presented here can accommodate a wide range of elastomers and elastomer deposition processes, as argued in [12]. The elastomer is degassed and cured, and this electrode stamping and elastomer deposition sequence is repeated until a multilayer stack with the desired number of layers has been achieved (Figs. 3G-M).

The stacks are cut out from the surrounding elastomer with a laser, leaving a thin insulating border surrounding the electrode (Fig. 3N). This may also be performed with a vinyl cutter or hand-cut with a craft knife and stencil. A craft

knife is then used to slice into the contact region, exposing cross-sections of the electrode (Fig. 3P), and conductive paint (PELCO Colloidal Graphite, Ted Pella) is applied to the cross-section to connect the electrode to external electronics (Fig. 3Q). Each of these stacks is then pre-cleared according to the process described in Sec. 3 to eliminate defects and ensure safe operation at high voltages. Each stack's capacitance is measured, and those with capacitance below 80% of the expected value are discarded.

These "mini stacks," are typically on the order of ten layers thick. This is enough for thinner DEAMs, but to achieve more layers mini stacks are typically assembled into "meta stacks" on the order of hundreds of layers. Mini stacks can be laminated together to create taller stacks as in [25], [26], and Fig. 1B. Alternatively, a single long stack may be rolled up to create a many-layered cylinder, as in [15] and Fig S16.

Our hybrid electrodes utilize the differing network topographies produced by CNT and CB inks where they are most advantageous. Fig. 1C diagrams a single "paddle" electrode of the same design pictured in Fig. 1A. CNTs are patterned over the active region of the electrode, i.e., the region which experiences the applied electric field. The sparse and fragile CNT networks that result, pictured in Fig. 1D, produce the desired self-clearing phenomenon that isolates short circuits. A small, 1 mm buffer region with only CNTs extends past the active region to prevent stray CB particles from precipitating breakdown in the active region. Unlike CNTs, CB forms larger and more durable agglomerates, as pictured in Fig. 1F. These aggregated CB networks are patterned at the contacts of the electrode, so that when a cut is made, ample cross-sectional area is exposed (Fig. 1J) for the conductive paint to connect to.

As seen in Fig. S17, the contact region comprises CNTs that are deposited atop the CB particles, draping over and connecting CB aggregates. This orientation is flipped when the electrodes are stamped onto the elastomer substrate. Fig. 1F shows how this results in CNTs being mostly obscured by the CB aggregates that now rest above them, but some CNTs can be seen between cracks in the CB layer. This CB+CNT architecture was used instead of CB alone to simplify the design of the electrodes and enhance conductivity of the contacts. Rather than attempt to determine the minimum overlap of CNT and CB regions to minimize any contact resistance at the transition pictured in Fig. 1E, we chose to simply cover the entirety of the CB with CNTs. This layered composite also enhances conductivity. A sheet resistance test specimen demonstrated that regions with CB alone had sheet resistances of 39.87 ± 1.79 kΩ/□ and those with CNTs alone measured 49.52 ± 4.92 kΩ/□. Assuming that these can be modeled as parallel resistances, we would expect the total sheet resistance to be 22.09 kΩ/□, but the measured resistance was 2.41 ± 0.29 kΩ/□, 9.16× lower than expected (n=3). This discrepancy is likely due to the increased connectivity that the added CNTs grant to the CB aggregates. As seen in the center of Figure 1F, this CNT layer can bridge cracks and other breaks in the CB network. A similar effect has been observed in silver nanowire-CNT composites [27]. The authors in [27] also noted that the deposition of distinct strata was necessary to achieve this performance increase – a simple mixture of the inks was insufficient.

To demonstrate that our fabrication process produces actuators with similar performance to that of previously described highly-tuned, well-proven processes, we replicated roll actuators from [24]. Remaking these actuators with hybrid electrodes made via our process, we achieved blocked forces within 13.6% of the results in [24] and free displacement within 1.5% (Sec. A.10.1). Supporting Movie 2 shows a roll actuator in operation.

3 Fully-defined, adaptive pre-clearing protocol enables safe and automated pre-clearing

After each mini-stack is fabricated, it is pre-cleared to its working voltage. This allows it to operate with little risk of a breakdown event occurring.

A pre-clearing algorithm must be able to both respond quickly to current spikes and perform high-level logic functions to analyze and adapt to heterogeneous failure events. We achieve this by splitting the algorithm across two timescales and two computers, as detailed in Fig. S1.

A target computer handles high-frequency (10 kHz) tasks with a Simulink model that has been compiled into C code. Before each episode, the host computer defines parameters of the desired pre-clearing voltage signal. During the episode, the target generates this signal and sends it to the data acquisition (DAQ) system (National Instruments PCI 6259). The target also monitors current draw via the DAQ– if current exceeds a set threshold, the voltage is immediately set to zero and the episode is terminated. This shutoff procedure allows us to limit the amount of energy that flows through a breakdown site. Fig. 4A illustrates how, within 1 ms of a current spike, the capacitor is fully discharged, and Fig. 4B shows how this limits damage to a small (< 100 µm) distance from the breakdown site. Once an episode terminates, either as a result of signal completion or earlier termination because of a current spike, the target sends all data from the episode to the host computer.

The host computer performs the high-level logic that allows it to adapt to heterogeneous failures resulting from the range of defects within and across devices. Upon the termination of an episode, the host evaluates whether and how the device failed during the episode, and based on this it specifies a signal for the next episode. This logic is diagrammed in Fig. S2, and can be expressed with only five binary decisions.

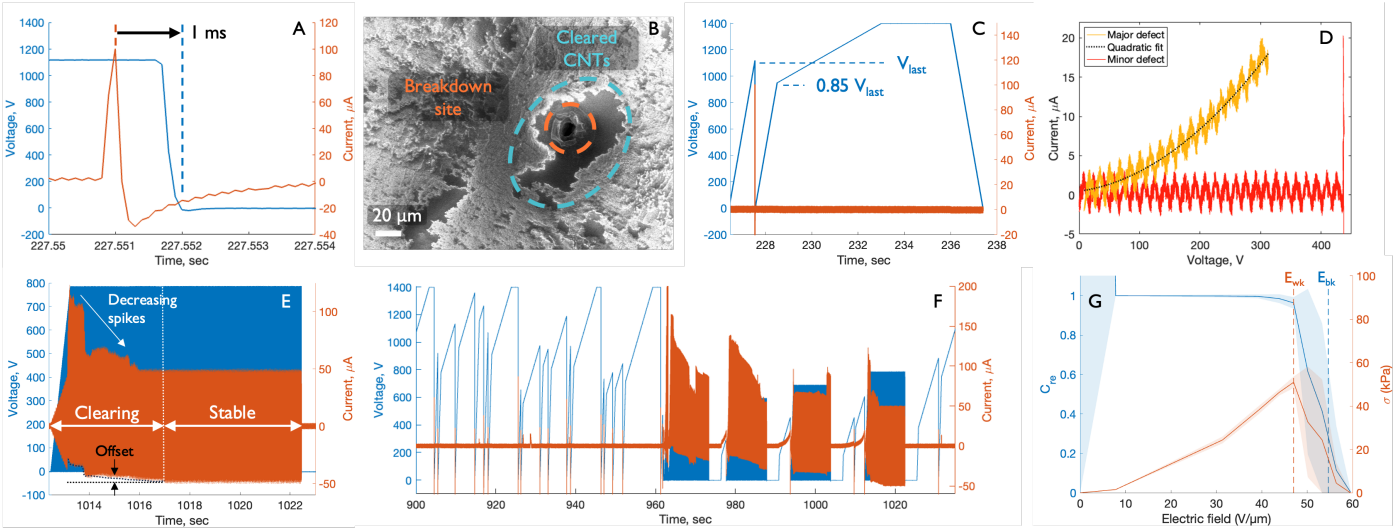

Figure 4: **Pre-clearing process. (A)** A current spike above 20 µA that triggers termination of a pre-clearing episode. The time between the spike and a full discharge is ∼1 ms. **(B)** SEM image of a breakdown site after a clearing event. The dark region around the pinhole has been cleared of CNTs, and is no longer conductive. **(C)** Two ramp and hold episodes. The first is terminated by a current spike at a voltage of V_{last}. The second ramp rises to $0.85V_{last}$ at 1000 V/s and then slows to 100 V/s. The ramp-and hold (and thus the pre-clearing process) completes successfully after holding the target voltage of 1400 V for three seconds. **(D)** Plot of the IV curves from episodes with major and minor failures. The major failure produces a quadratic dependence of current on voltage. The minor failure, in contrast, produces a sudden spike in current, seen at ∼450V. **(E)** An AC burst successfully clearing a major defect. An initial clearing period evidenced by current spikes and offsets is followed by a stable period. **(F)** An example section of a pre-clearing procedure. After initial ramp-and-hold episodes, a major failure is detected. The program adapts to clear the failure by progressively increasing the burst voltage from 500 to 780 V. A ramp-and-hold is employed after each burst to assess whether the short has been cleared. Once it is clear, the program reverts to ramp-and-hold episodes. **(G)** Capacitance retention and estimated output stress after each pre-clearing voltage for n=12 hybrid-electrode breakdown devices. Shaded regions indicate ±1 SD. The maximum predicted stress $\sigma = 51$ kPa occurs at 47.0 V/μm, before the breakdown strength 54.7 V/μm is reached. The high variation in C_{re} at 0 V is an artifact of initial conductive paths through the dielectric layer before preclearing, possibly from stray NPs. All measurements in (A-G) were taken from single-layer, paddle-shaped DEAs.

For the first episode, the pre-clearing algorithm attempts a "ramp and hold" strategy. The ramp and hold strategy pictured in Fig. 4C applies a linear ramp of 1000 V/s to the DEA. Once the ramp reaches 85% of the last voltage that was reached, the ramp slows to 100 V/s. The high initial slew rate makes the process time-effective, and the lower subsequent rate prevents excessive damage as the voltage approaches the previous breakdown threshold. As previously discussed, prior work has generally applied clearing voltages in relatively large steps of tens to hundreds of volts [1,15,16] which can cause excessive degradation. The 100 V/s ramp is much more conservative; given the 10 kHz sampling rate of the DAQ, steps of 10 mV are theoretically possible. Practically, however, the total measured noise is typically ∼1 V, still one to two orders of magnitude smaller than previous efforts. Once the voltage reaches its target level, it is held for three seconds. If no current spike is detected, the process is considered complete and the device is successfully pre-cleared.

If a current spike above 20 µA is detected during the process, however, the current episode is immediately terminated by the target computer and the voltage is set to zero. 20 µA was chosen as the threshold because it is the minimum approximate current needed to destroy a single CNT [17], and it is sufficiently higher than the Trek 610E amplifier's current monitor noise floor of approximately 3 µA. Once the episode is terminated, the host computer's program examines the current-voltage (I-V) curve to determine what type of failure occurred. As pictured in Fig. 4D, there are two types: a sudden spike in current, and a gradual increase in current as a function of voltage. The former indicates a "minor defect". A single minor defect does not measurably affect the device's capacitance or resistance. A "major defect", however, causes a durable short-circuit through a dielectric layer. This short-circuit causes a quadratic increase in current with applied voltage, so the program detects these shorts by attempting a quadratic curve fit of the I-V curve. If the fit is good ($R^2 > 0.85$) and the curve is concave-up, the program identifies the current increase as an indicator of a major defect, and a short detection flag is set. The superlinear increase in current with voltage suggests that the voltage is changing the resistance of the short-circuit; this may be the result of increasing voltage allowing for current to cross

an increasing number and size of nanoscale gaps proximal to the breakdown site, increasing conductivity.

Ramps cannot be used to effectively clear these major defects; 20 µA is not enough current to clear them, but using a higher current limit creates a positive feedback loop: more current further damages the dielectric, making it more conductive and requiring more current to clear. These major defects may be spots of high CNT concentrations, as excessive CNT concentration has been shown to prevent effective clearing [13, 15, 18]. To break this conductivity-current positive feedback loop, a high-frequency (100 Hz) sinusoid is applied to the device for 10 seconds. Previous work has demonstrated that limiting the pulse width of a clearing signal can enhance breakdown strength [13]. Our "AC burst" signal similarly applies short bursts of high current to the device, limiting the amount of energy that can flow through the defect in a single cycle. Figure 4E shows an AC burst used to clear a major defect in a single-active-layer device with the geometry shown in Fig 1C. At the beginning of the episode, the peak current I_{max} is approximately 120 µA, and the current signal is positively offset, reflecting current through the defect(s). As defects are cleared, I_{max} stabilizes at 47 µA. This stable current can be estimated by the current required to charge an ideal capacitor

$$\hat{I}_{max} = \pi f V_{max} C \tag{1}$$

where f and V_{max} are the frequency and peak-to-peak voltage of the applied signal, respectively, and C is the capacitance of the device. For the 780 V, 100 Hz signal applied to the 134 pF device tested, $\hat{I}_{max}$=33 µA. The 30% discrepancy between I_{max} and $\hat{I}_{max}$, possibly due to non-ideal behavior of the DEA, makes it an unreliable indicator of clearing success or failure, but it is useful for estimating how high of a current limit to set during the AC burst process. AC burst signals can still damage a device if not carefully limited, so the limit is set to approximately 200 µA more than the current needed to charge the capacitor, $\hat{I}_{max}$.

The AC burst strategy is adaptive; if the episode completes without exceeding the current limit, V_{max} is increased by ∼15% for the next AC burst, and if it does not then V_{max} is reduced by ∼37%. This adaptability is necessary to automate the pre-clearing procedure; there is wide variation in the voltage required to clear a major defect, and this algorithm ensures that the minimum possible voltage is used, minimizing damage. The approximate nature of the increases and reductions is due to a random prefactor. This prefactor, uniformly distributed from 0.975 to 1.025, ensures that the AC burst pre-clearing process does not become trapped in a deterministic sequence of applied voltages that cannot clear the defect, instead exploring the solution space for a suitable voltage. After the burst has completed, a three-second rest period allows thermal energy near the defect to dissipate.

Each AC burst is followed by a ramp and hold episode, as shown in Fig 4F. This allows the program to assess whether the short was successfully cleared and take appropriate action. If an over-current event occurs and a short is still detected, an AC burst is again deployed. If a short is no longer detected, the short detection flag is unset, and V_{max} is reset to its default value (500 V). This reset prevents the program from applying more than the minimum voltage to the next short. AC bursts are also deployed to hasten the pre-clearing process. Occasionally, the pre-clearing process becomes "stuck" around a certain voltage, with each ramp failing at the same voltage. If more than four ramps fail within 25 V of each other, the algorithm uses the adaptive AC burst strategy to quickly clear the associated defects.

The entire pre-clearing process typically takes 1-10 min for devices with a capacitance of 100-1000 pF. Generally, larger-capacitance devices take longer to clear, as the number of defects scales with total electrode area and device volume.

Pre-clearing is a balance between increasing device output and limiting degradation. Increasing the target clearing voltage allows for a higher working field E_{wk} during operation, but as more defects clear with increasing clearing field, the accumulated damage reduces the effective area of the electrodes. This degradation can be described with capacitance retention (C_{re}), the ratio of current to initial device capacitance [13]. After each target voltage is applied, the capacitance can be measured with an LCR meter (Agilent E4980A). As Fig. 4G illustrates, C_{re} is generally stable until reaching a threshold at which it suddenly declines as clearing events become more numerous and severe. In order to maximize output stress, $C_{re}E^2$ has been proposed as the objective function to maximize [13]. We similarly choose to maximize output stress, but add additional terms to estimate the device's output stress σ as

$$\sigma = C_{fe} C_{re} \epsilon E^2 \tag{2}$$

where ϵ is the elastomer's permittivity, E is the applied field, and C_{fe} is the ratio of measured capacitance after fabrication to the expected capacitance $\frac{A\epsilon}{H}$, where A is the area of each electrode and H is the thickness of the dielectric between them. C_{fe} accounts for fabrication errors such as the incomplete coverage of the electrode seen in Fig 1D.

The external interfaces at the CB+CNT contacts are robust to electrical cycling during pre-clearing. As seen in Fig 4E, each of the 100-Hz bursts last for up to 10 seconds, or 1000 cycles. Pre-clearing a single-layer paddle-shaped DEA to the working field typically requires approximately 1-10 AC bursts and 100-1000 ramp-and-hold episodes, representing 1,000-10,000 and 100-1,000 actuation cycles, respectively. As seen in Fig S3, as pre-clearing progresses, the average resistance of devices does not notably change; the mean resistance of devices after pre-clearing to the working field of 47.0 V/µ(1500 V) is within 1.5% of the mean after eliminating initial short-circuits in the as-manufactured devices.

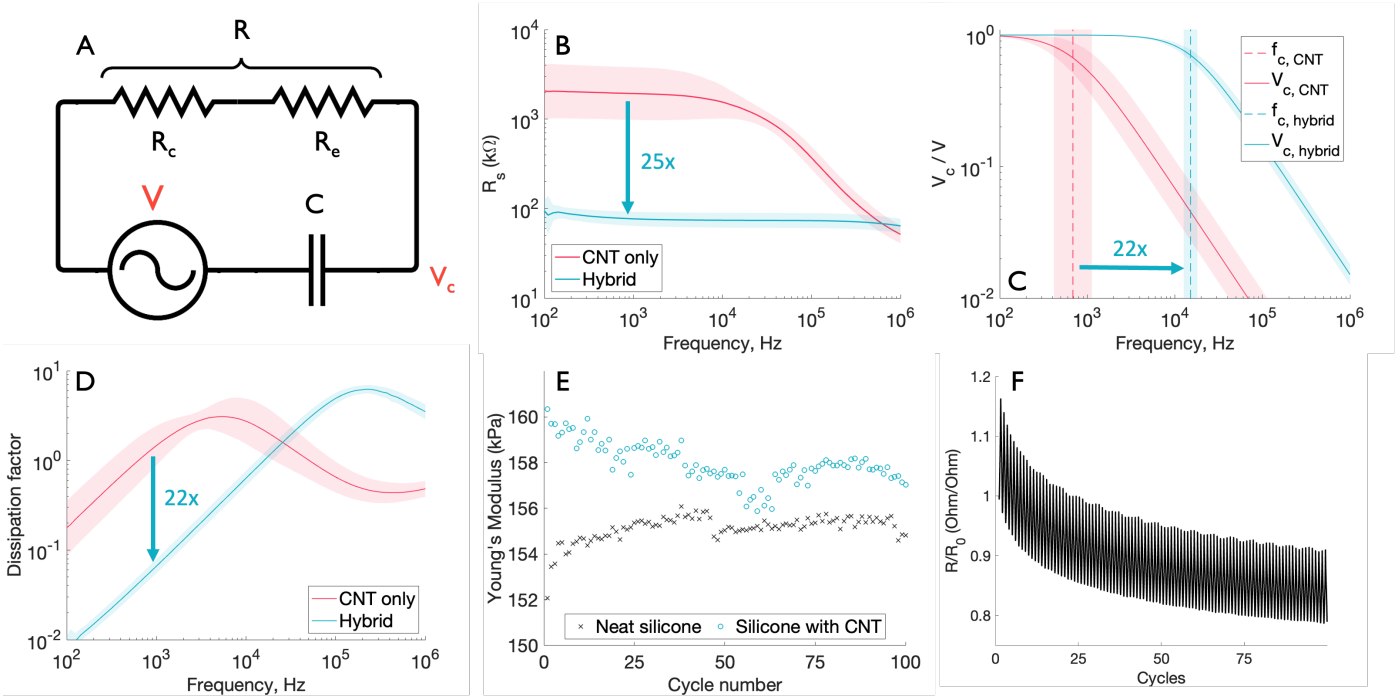

Figure 5: **Resistive performance of hybrid electrodes. (A)** Circuit model of the DEA. The total resistance R is the sum of contact resistance R_c and the resistance through the body of the electrode R_e. **(B)** Comparison of resistance as a function of frequency for n=12 hybrid and 12 CNT-only devices. **(C)** Comparison of voltage across the capacitor between CNT-only and hybrid electrodes as a function of frequency. **(D)** Dissipation factor as a function of frequency for DEAs with hybrid vs CNT-only electrodes. Lines in B-D represent the mean, and shaded error bounds represent ± 1 SD_{log}. **(E)** Measured Young's modulus as a function of cycle number for neat silicone and silicone with CNT electrodes. **(F)** The ratio of measured resistance R to initial measured resistance R_0 of a CNT electrode sample as it is stretched between 5% and 25% strain.

4 Reduced contact resistance increases bandwidth and efficiency

We model the resistance of an electrode R as the sum of its contact resistance R_c and the resistance from the body of the electrode R_e (Fig. 5A). Given the CNTs' sheet resistance of 49.52 kΩ/□, electrode designs with an aspect ratio on the order of unity have an R_e on the order of 100 kΩ. This resistance, however, is typically dominated by CNTs' contact resistance. As shown in Fig S5A, R_c is 284.9 ± 151.3 kΩ (mean ± 95% CI) for a 5 mm-long contact. Adding CB (Fig S5B) reduces this resistance R_c by 32× to 8.817 ± 3.649 kΩ, making R_e the dominant resistance and lowering R to approximately the value of R_e.

Fig 5B shows this effect for n=12 single-DEA-layer, paddle-shaped test devices with CNT only vs CB+CNT contacts. Each device was originally manufactured as a hybrid-electrode device and pre-cleared to 250 V (7.84 V/μm) to eliminate initial short-circuits, and then capacitance and resistance measurements were taken on an LCR meter. This yielded a mean resistance of 76.8 kΩ at 1000 Hz. After taking measurements with CB+CNT contacts, the contacts were remade by slicing through the CNT-only portion of the tab and discarding the CB+CNT composite contacts, as diagrammed in Fig S14. When the connections were remade in the CNT-only region, the mean resistance increased to 1930 kΩ. This indicates that R_c strongly dominates R for CNT-only electrodes. CNT-only contacts are not only more resistive, but also far more variable. This is possibly due to the sparse topography of CNT networks relative to CB networks shown in Figs 1D-F leading to large variations in local cross-sections (Figs 1G-J) and sensitivity to cut conditions. The range of resistances within 1 SD_{log} of the mean (calculation described in Sec A.6) increases from [64.2, 92.0] kΩ for CB+CNT contacts to [981, 3800] kΩ for CNT-only contacts. This variability, also exhibited in contact resistance measurements in Fig S5A, makes electrical analysis of CNT-only electrodes challenging. Estimating the difference between contact resistances as the difference in total resistances between CNT- and composite-contact devices yields $\Delta R_c = 1853$ kΩ, while the difference between contact resistances measured with dedicated tests was $\Delta R_c = 276.1$ kΩ. This difficulty is compounded by the potential impact of other factors such as elastomer compliance, the effect of pre-clearing, and environmental variability.

This lower contact resistance increases the electrical cutoff frequency of devices from 0.586 to 15.1 kHz (Fig 5C),

enabling high-frequency applications such as audio drivers which must actuate at tens of kHz. We define the cutoff frequency f_c as the frequency at which the voltage across the dielectric drops to -3 dB (∼70%) of the applied voltage. This can be calculated as

$$f_c = \frac{1}{2\pi RC} \tag{3}$$

assuming that the circuit can be modeled as depicted in Fig. 5A: a resistance, R, in series with a capacitance, C. Fig. S4 demonstrates how this simple model sufficiently captures the circuit's behavior.

The decreased resistance also enhances efficiency. Fig 5D illustrates its effect on the dissipation factor D, which represents the ratio of real to reactive power in the DEA. At 1000 Hz, more power is lost to resistance than is oscillating reactively in a CNT-only device ($D_{CNT} = 1.49$), whereas less than a tenth is lost in a hybrid device ($D_{hybrid} = 0.067$). This 22× efficiency boost allows for smaller associated batteries and power electronics, enabling applications in compact consumer electronics and untethered micro-scale vehicles [16].

The reduction in resistance is highly dependent on electrode geometry, however. While the paddle-shaped devices saw a 22× reduction in contact resistance by adding CB to the contacts, a roll actuator of the design presented in [15,24] saw only a 3% reduction from 39.2 to 38.2 kΩ. While these results are complicated by changes in manufacturing and pre-clearing process, this small difference is likely due in large part to differences in electrode contact length; the roll actuator electrodes were designed to minimize the influence of contact resistance by running the contacts along the entirety of the actuator's 50 mm length. In contrast, the paddle-shaped electrodes are designed with a small 5 mm contact length. This contact width must be kept small: for a stacked actuator, the contact regions are along the direction of actuation rather than at fixed attachment points at the end of a roll, thus low contact widths limit additional mechanical impedance. Therefore, the total resistance of paddle-shaped electrodes is far more sensitive to changes in contact resistance than is that of the roll actuators. Hybrid electrodes with composite CB+CNT contacts thus provide the greatest benefit to devices that require smaller contacts in order to either reduce mechanical impedance or increase design freedom; instead of creating a wide contact co-located with the edge of the active region of the device, a designer could create a short contact that is located more conveniently on another part of the actuator or an integrated assembly that is mechanically isolated from active regions experiencing high strains.

To study the effects of cyclic strain on the electromechanical behavior of the electrodes, a single electrode layer was transferred onto a silicone film and then encapsulated, yielding a specimen 60 μm thick, 50 mm long, and 10 mm wide. The specimen was mounted onto a polystyrene frame with silicone adhesive to aid in removal of the specimen from the acrylic platter used for spin-coating. The specimen was then installed in a uniaxial tensile testing machine (Instron 68TM-10) which applied 100 cycles of strain from 5% to 25% while recording load and displacement. The resistance of the electrode was simultaneously measured using a digital multimeter (Keysight 34465A). The mechanical and electrical data was then aligned manually during post-processing.

We have previously shown that batch-sprayed and stamped CB electrodes [12] contribute negligible stiffness, and we similarly show that the CNT networks similarly add negligible stiffness to the active region of the hybrid electrodes ($Y_{electrode} = (1.062 \pm 0.049) \times Y_{neatsilicone}$, mean ± standard deviation, $n = 4$). The stress-strain curves and evolution of Young's modulus for representative samples are shown in Fig. 5E (additional samples included in Section A.5.1).

When subjected to cyclic extension from 5% to 25% strain (similar to strains expected during operation), we observed that the resistance of the electrodes has a close-to-linear response to applied strain and that the resistance of the electrode decreases relative to its initial resistance, similar to behavior shown by Kim, *et al.* [28] which we surmise to be due to alignment of the CNTs in the direction of stretching [29] (Fig. 5F and S7). When subjected to cyclic strain over a range of 100%, the resistance increased relative to its initial value (Fig. S8).

5 CNT-only active regions maintain breakdown strength and actuator output

The electrodes of a DEA can strongly affect its breakdown strength and behavior. They introduce defects into the device that lower its strength compared to that of the neat material. CB electrodes, for example, have been shown to lower breakdown strength by 16-36% compared to neat silicone [22,30].

Breakdown has typically been defined in literature as a sudden, steep, and irreversible increase in leakage current across the dielectric [31]. This "hard breakdown" can thus be characterized as binary: failed or not failed, and the field at which the failure occurs is denoted as a specimen's breakdown field. These fields are fit to a Weibull distribution [32], and the breakdown strength of the batch is taken to be the field at which there is a $1 - e^{-1}$ chance of failure. As discussed earlier, however, CNT-based electrodes do not fail quickly and catastrophically. Rather, they fail in a series of self-clearing events that incrementally degrade their capacitances and thus actuation outputs. To provide a comparison to other breakdown statistics, we thus define the failure of an individual device as the electric field at which capacitance

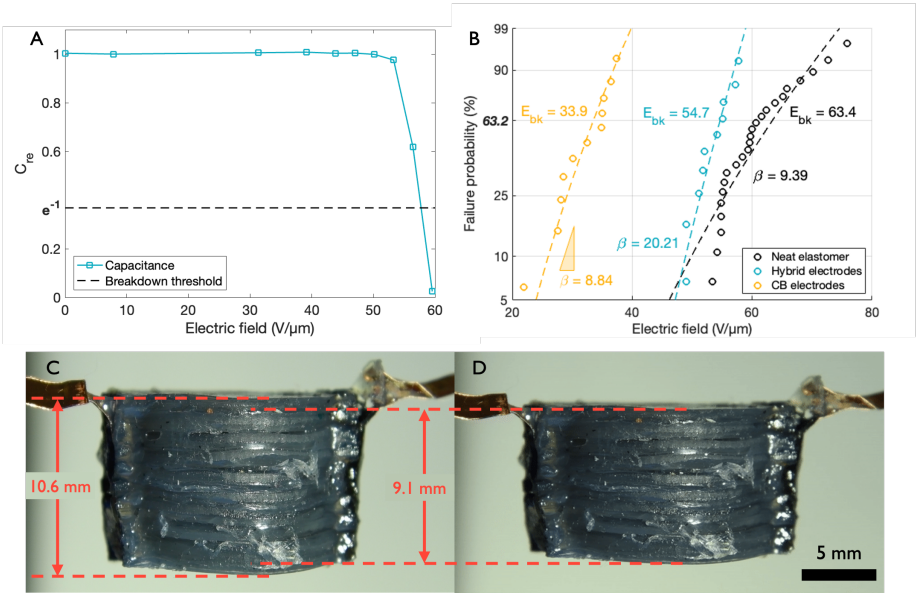

Figure 6: **Breakdown strength and its effect on device output. (A)** Measurement of a single device's breakdown field. The device is pre-cleared to a series of increasing electric fields using the adaptive pre-clearing algorithm described in this work. Each point is the capacitance retention C_{re} of the device which is measured after each field has been applied. Breakdown is taken to be the nominal applied field at which C_{re} drops below the threshold of e^{-1}. **(B)** Weibull plot of breakdown strengths of CB electrodes from [12], hybrid electrodes, and neat P7670 with no electrodes [12]. Each point represents one device's breakdown field. The points are fit to Weibull distributions, which estimate the probability of failure for a given applied field. For the neat elastomer (n=25) and CB-electrode devices (n=11), voltage was slowly ramped up, and each device's breakdown field was taken as the nominal field at which catastrophic failure of the dielectric occurred, as indicated by a sharp and irreversible surge in current. This method is detailed in [12]. For the hybrid electrodes (n=12), each device's breakdown field was determined by the method demonstrated in (A). The dielectric in each device is a 32 µm thick layer of Elastosil P7670. β is the slope of the curve in Weibull-space, and indicates consistency. **(C)** An unactuated 100-layer DEAM in the free displacement condition. **(D)** Maximum (14%) compression of the DEAM upon applying a 1 Hz, 3100 V_{pp} sinusoid.

retention C_{re}, the ratio of current to original capacitance, drops to e^{-1} (Fig 6A). Our definition of device breakdown strength can thus be approximately understood as the applied field at which $\frac{2}{3}$ of devices lose at least $\frac{2}{3}$ of their output.

Figure 6B shows how hybrid electrodes utilizing self-clearing CNTs in active regions achieve superior breakdown strength to CB-only electrodes from our previous work (54.7 vs 33.5 V/μm) [12]. This is 86.4% of their upper limit, the breakdown strength of neat P7670 (63.4 V/μm). In addition, they achieve higher consistency ($\beta_{hybrid} = 20.21$) than either our previous CB electrodes ($\beta_{CB} = 8.84$) or the neat elastomer ($\beta_{neat} = 9.39$) [12]. This high strength and consistency, along with the non-catastrophic self-clearing mechanisms of CNT networks, allows for the scaling of high performance to larger DEAMs.

As previously described, the batch spray process makes it easy to scale the number and size of DEA layers. This allows for the enhanced stresses and strains to be scaled to produce large forces and displacements. We demonstrate this with an artificial muscle 1.5 cm in diameter, 1 cm thick, with 100 active layers (Figure 6E). In free displacement and with an applied field of 45 V/μm, this device achieves 1.5 mm of displacement (14% strain) through its thickness, as shown in Figure 6F and in Supporting Movie 3. To evaluate blocked force output, we pre-compressed the stack by approximately 1.5 mm and measured the amount of force relaxed during actuation at 45 V/μm. The device produced 6.9 N of force (39 kPa), 260× its own weight. This compares favorably with previous devices with similar elastomers that achieved 5% strain and 35 kPa stress at a similar applied field (48 V/μm) [33]. It is also within 14% of the expected value of 8.0 N calculated by Equation (2) for this device. The ratio of the measured capacitance as-fabricated to expected capacitance values of the stack was $C_{fe} = 0.86$, which may be due to such factors as incomplete coverage of CNTs and misalignment during the stacking process. This accounting is enumerated in Section A.9.2.

6 Discussion and conclusion

In this work, we demonstrate that spatially-patterned hybrid electrodes can improve the performance of existing DEAMs. Hybrid electrodes can achieve low contact resistances without sacrificing high breakdown strength, and vice versa. We

also present practical methods of fabricating and pre-clearing these hybrid electrodes that enable their development and deployment at scale.

We have demonstrated the ability to modularly pattern distinct properties across an electrode by patterning distinct nanoparticle inks. This modularity allows designers to take advantage of nanoparticles' unique advantages and avoid their disadvantages, reducing the difficulty of development while increasing performance.

We leverage this novel capability to resolve a previously fundamental tradeoff between breakdown strength and contact resistance in DEAMs made with nanoparticle electrodes. We demonstrate that CB placed at the contacts can reduce contact resistance by 32× while self-clearing CNTs patterned in active regions of the electrode can maintain high breakdown strengths (54.7 V/μm) that approach the strength of neat elastomer (63.4 V/μm). The high breakdown strength results in muscle-like stresses of 39 kPa and muscle-like strains of 14%. Its consistency ($\beta = 20.21$) also allows us maintain this in a centimeter-scale artificial muscle with 100 DEA layers. The low contact resistance makes DEAMs 26× faster and 22× more efficient than those with CNT-only electrodes, making higher-frequency and untethered use cases of more viable for DEAMs. The lower contact resistance also reduces the need for long contacts such as those used in roll actuators, expanding the range of actuator designs and possible applications.

The CNT ink formulation and deposition parameters have not been extensively tuned; future work may do so in order to achieve higher performance. CNT concentration has previously been shown to have a strong effect on breakdown strength [13, 16], so further optimization may yield breakdown strengths closer to the limit set by the neat material. Similarly, optimization of spray deposition parameters such as vacuum strength and spray pattern may yield superior homogeneity and thus higher conductivity and/or breakdown strength in CNT regions. The breakdown strength of Elastosil P7670 (63.4 V/μm), however, limits the achievable breakdown strength of the DEAMs manufactured with it. Recent work has demonstrated elastomers with breakdown strengths as high as 330 V/μm that do not require mechanical prestretch [4]. Because our electrode fabrication process is agnostic to the elastomer used, such high-performance dielectrics could be substituted to dramatically increase the stresses and strains produced by DEAMs. Tuning fabrication parameters such as mask thickness and alignment methods may also allow for smaller features and reduced buffer zones, enabling millimeter- and micron-scale devices.

While in this work we use CB and CNT-based inks, future inks and the capabilities that stem from them would be relatively easy to implement. The batch-spray and stamp process depends only minimally on ink and substrate material properties, allowing for quick development and deployment of novel inks. These inks could provide additional functionalities such as optical switching for on-the-fly rewiring [34, 35], high transparency or opacity for optical modification [9], low sheet resistance for power distribution [27], or electroluminescence for status monitoring and communication [36].

The electrode fabrication method not only reduces development time and improves device performance; it is also cheap and easily scalable. The materials costs are low – a 220×220 mm sheet of patterned electrodes requires only $6.87, mostly from the cost of the filter paper (Section A.8). Future work may investigate filter paper reuse and spray toolpath tuning to further reduce material costs. The batch-spray and stamp-transfer paradigm allows for virtually unlimited electrode area, and both electrode deposition and transfer operations could be implemented at high throughput in a roll-to-roll process. This scalability makes manufacturing of many-layered artificial muscles and large-area rolls possible, allowing high stresses and strains to be converted into large forces and displacements. Larger actuators could be used to drive mechanisms for higher load tasks such as electroadhesion, electrostatic clutching, mechanical counterpressure, and stiffness variation [37–41]. The throughput of the manufacturing process, however, is currently limited by the elastomer deposition step. Each active layer requires the elastomer to be spin-coated, degassed, cured, and cooled. This process currently requires approximately 30 minutes per layer. Similarly to how BSS processes batch-produce electrodes and then quickly stamp them, throughput could be improved by batch-producing dry films and quickly laminating them together, as proposed in [4, 42].

We also developed an algorithm for safely pre-clearing CNT- and hybrid-electrode DEAMs and implemented it on a high-speed, automated system. We show how an AC waveform applied to the DEA can clear away major defects, while a DC ramp waveform is useful for clearing minor defects. Moreover, we develop a simple discriminant for detecting major defects based on a quadratic dependence of current on voltage. We implement these techniques on a target computer which can run at 10 kHz, allowing for fast detection and response to current spikes. With this added safety and adaptability, no human supervision is required and clearing can be completed quickly (∼1-10 minutes) and automatically, potentially enabling industrial-scale production of DEAMs and the acceleration of DEAM research.

Many of the values used for pre-clearing, however, were chosen heuristically. Future work should more systematically investigate the sensitivity of device performance parameters to various pre-clearing parameters such as current limits and the frequency of AC bursts. This may lead not just to further gains in performance but an increased understanding of the phenomena underlying pre-clearing. In the longer term, these phenomena should be explored in depth – a more causal understanding of how defects lead to failure may guide the development of superior manufacturing and pre-clearing techniques that mitigate the effects of these defects.

References

[1] M. Duduta, E. Hajiesmaili, H. Zhao, R. J. Wood, and D. R. Clarke, "Realizing the potential of dielectric elastomer artificial muscles," *Proceedings of the National Academy of Sciences of the United States of America*, vol. 116, no. 7, pp. 2476–2481, 2019.

[2] R. Heydt, R. Kornbluh, J. Eckerle, and R. Pelrine, "Sound radiation properties of dielectric elastomer electroactive polymer loudspeakers," *Smart Structures and Materials 2006: Electroactive Polymer Actuators and Devices (EAPAD)*, vol. 6168, p. 61681M, 2006.

[3] X. Ji, X. Liu, V. Cacucciolo, M. Imboden, Y. Civet, A. E. Haitami, S. Cantin, Y. Perriard, and H. Shea, "An autonomous untethered fast soft robotic insect driven by low-voltage dielectric elastomer actuators," *Science Robotics*, vol. 4, no. 37, 2019.

[4] Y. Shi, E. Askounis, R. Plamthottam, T. Libby, Z. Peng, K. Youssef, J. Pu, R. Pelrine, and Q. Pei, "A processable, high-performance dielectric elastomer and multilayering process," *Science*, 7 2022. [Online]. Available: https://www.science.org

[5] G. Kovacs, L. Düring, S. Michel, and G. Terrasi, "Stacked dielectric elastomer actuator for tensile force transmission," *Sensors and Actuators A: Physical*, vol. 155, no. 2, pp. 299–307, 10 2009. [Online]. Available: https://www.sciencedirect.com/science/article/pii/S0924424709004002#bib14

[6] P. Lotz, M. Matysek, and H. F. Schlaak, "Fabrication and Application of Miniaturized Dielectric Elastomer Stack Actuators," *IEEE/ASME Transactions on Mechatronics*, vol. 16, no. 1, pp. 58–66, 2 2011. [Online]. Available: http://ieeexplore.ieee.org/document/5677501/

[7] J. Shintake, S. Rosset, B. E. Schubert, D. Floreano, and H. Shea, "A Foldable Antagonistic Actuator," *IEEE/ASME Transactions on Mechatronics*, vol. 20, no. 5, pp. 1997–2008, 2015.

[8] E. Hajiesmaili and D. R. Clarke, "Dielectric elastomer actuators," *Journal of Applied Physics*, vol. 129, no. 15, pp. 1–38, 2021.

[9] S. Shian, R. M. Diebold, A. McNamara, and D. R. Clarke, "Highly compliant transparent electrodes," *Applied Physics Letters*, vol. 101, no. 6, 8 2012.

[10] M. Duduta, R. J. Wood, and D. R. Clarke, "Multilayer Dielectric Elastomers for Fast, Programmable Actuation without Prestretch," *Advanced Materials*, vol. 28, no. 36, pp. 8058–8063, 2016.

[11] S. Schlatter, G. Grasso, S. Rosset, and H. Shea, "Inkjet Printing of Complex Soft Machines with Densely Integrated Electrostatic Actuators," *Advanced Intelligent Systems*, vol. 2000136, p. 2000136, 2020.

[12] A. J. Cohen, M. Kollosche, M. C. Yuen, D.-y. Lee, D. R. Clarke, and R. J. Wood, "Batch-sprayed and stamp-transferred electrodes: a new paradigm for scalable fabrication of multilayer dielectric elastomer actuators," *Advanced Functional Materials*, 2022.

[13] S. Jiang, C. Tang, X. J. Liu, and H. Zhao, "Long-Life-Cycle and Damage-Recovery Artificial Muscles via Controllable and Observable Self-Clearing Process," *Advanced Engineering Materials*, vol. 2101017, pp. 1–11, 2021.

[14] S. Kim, Y.-H. Hsiao, Y. Lee, W. Zhu, Z. Ren, F. Niroui, and Y. Chen, "Laser-assisted failure recovery for dielectric elastomer actuators in aerial robots," *Science Robotics*, 2023. [Online]. Available: https://www.science.org

[15] H. Zhao, A. M. Hussain, M. Duduta, D. M. Vogt, R. J. Wood, and D. R. Clarke, "Compact Dielectric Elastomer Linear Actuators," *Advanced Functional Materials*, vol. 1804328, pp. 1–12, 2018.

[16] Z. Ren, S. Kim, X. Ji, W. Zhu, F. Niroui, J. Kong, and Y. Chen, "High Lift Micro-Aerial-Robot Powered by Low Voltage and Long Endurance Dielectric Elastomer Actuators," *Advanced Materials*, p. 2106757, 2021.

[17] P. G. Collins, M. S. Arnold, and P. Avouris, "Engineering Carbon Nanotubes and Nanotube Circuits Using Electrical Breakdown," *Science*, 2001. [Online]. Available: https://www.science.org

[18] W. Yuan, L. Hu, Z. Yu, T. Lam, J. Biggs, S. M. Ha, D. Xi, B. Chen, M. K. Senesky, G. Grüner, and Q. Pei, "Fault-tolerant dielectric elastomer actuators using single-walled carbon nanotube electrodes," *Advanced Materials*, vol. 20, no. 3, pp. 621–625, 2 2008.

[19] S. Xu, C. M. Nunez, M. Souri, and R. J. Wood, "A compact DEA-based soft peristaltic pump for power and control of fluidic robots," *Science Robotics*, 2023. [Online]. Available: https://www.science.org

[20] Y. Chen, S. Xu, Z. Ren, and P. Chirarattananon, "Collision resilient insect-scale soft-actuated aerial robots with high agility," *IEEE Transactions on Robotics*, vol. 37, no. 5, pp. 1752–1764, 2021.

[21] X. Ji, X. Liu, V. Cacucciolo, Y. Civet, A. El Haitami, S. Cantin, Y. Perriard, and H. Shea, "Untethered Feel-Through Haptics Using 18-µm Thick Dielectric Elastomer Actuators," *Advanced Functional Materials*, vol. 2006639, pp. 1–10, 2020.

[22] B. Fasolt, F. B. Albuquerque, J. Hubertus, G. Schultes, H. Shea, and S. Seelecke, "Electrode Impact on the Electrical Breakdown of Dielectric Elastomer Thin Films," *Polymers*, vol. 15, no. 20, 10 2023.

[23] O. Araromi, A. Conn, C. Ling, J. Rossiter, R. Vaidyanathan, and S. Burgess, "Spray deposited multilayered dielectric elastomer actuators," *Sensors and Actuators A: Physical*, vol. 167, no. 2, pp. 459–467, 6 2011. [Online]. Available: https://www.sciencedirect.com/science/article/pii/S0924424711001312

[24] S. Xu, Y. Chen, N. S. P. Hyun, K. P. Becker, and R. J. Wood, "A dynamic electrically driven soft valve for control of soft hydraulic actuators," *Proceedings of the National Academy of Sciences of the United States of America*, vol. 118, no. 34, 2021.

[25] J. Maas, D. Tepel, and T. Hoffstadt, "Actuator design and automated manufacturing process for DEAP-based multilayer stack-actuators," *Meccanica*, vol. 50, no. 11, pp. 2839–2854, 2015.

[26] D.-y. Lee, S. H. Jeong, A. J. Cohen, D. M. Vogt, M. Kollosche, G. Lansberry, Y. Mengüç, A. Israr, D. R. Clarke, and R. J. Wood, "A wearable textile-embedded dielectric elastomer actuator haptic display," *Soft Robotics*, 2022.

[27] Y. R. Lee, H. Kwon, D. H. Lee, and B. Y. Lee, "Highly flexible and transparent dielectric elastomer actuators using silver nanowire and carbon nanotube hybrid electrodes," *Soft Matter*, vol. 13, no. 37, pp. 6390–6395, 2017.

[28] J. H. Kim, J.-Y. Hwang, H. R. Hwang, H. S. Kim, J. H. Lee, J.-W. Seo, U. S. Shin, and S.-H. Lee, "Simple and cost-effective method of highly conductive and elastic carbon nanotube/polydimethylsiloxane composite for wearable electronics," *Scientific Reports*, vol. 8, no. 1, p. 1375, Jan. 2018, number: 1 Publisher: Nature Publishing Group. [Online]. Available: https://www.nature.com/articles/s41598-017-18209-w

[29] Z. Tang, Q. Huang, Y. Liu, Y. Chen, B. Guo, and L. Zhang, "Uniaxial Stretching-Induced Alignment of Carbon Nanotubes in Cross-Linked Elastomer Enabled by Dynamic Cross-Link Reshuffling," *ACS Macro Letters*, vol. 8, no. 12, pp. 1575–1581, Dec. 2019, publisher: American Chemical Society. [Online]. Available: https://doi.org/10.1021/acsmacrolett.9b00836

[30] B. Fasolt, F. Welsch, M. Jank, and S. Seelecke, "Effect of actuation parameters and environment on the breakdown voltage of silicone dielectric elastomer films," *Smart Materials and Structures*, vol. 28, no. 9, 8 2019.

[31] D. Gatti, H. Haus, M. Matysek, B. Frohnapfel, C. Tropea, and H. F. Schlaak, "The dielectric breakdown limit of silicone dielectric elastomer actuators," *Applied Physics Letters*, vol. 104, no. 5, 2 2014.

[32] B. Waloddi Weibull, "A Statistical Distribution Function of Wide Applicability," *Journal of Applied Mechanics*, 1951.

[33] A. Behboodi and S. Lee, "Benchmarking of a Commercially Available Stacked Dielectric Elastomer as an Alternative Actuator for Rehabilitation Robotic Exoskeletons," in *2019 IEEE 16th International Conference on Rehabilitation Robotics (ICORR)*, Jun. 2019, pp. 499–505, iSSN: 1945-7901.

[34] E. Hajiesmaili and D. R. Clarke, "Optically addressable dielectric elastomer actuator arrays using embedded percolative networks of zinc oxide nanowires," *Materials Horizons*, vol. 287, no. 5454, 10 2022.

[35] C. Gillespie, A. Marzo, F. Scarpa, J. Rossiter, and A. T. Conn, "High-voltage photonic switching of dielectric elastomers with amorphous silicon thin-films," in *Electroactive Polymer Actuators and Devices (EAPAD) XXI*, vol. 10966. SPIE, Mar. 2019, pp. 283–288.

[36] S. Kim, Y. H. Hsiao, Y. F. Chen, J. Mao, and Y. F. Chen, "FireFly: An Insect-Scale Aerial Robot Powered by Electroluminescent Soft Artificial Muscles," *IEEE Robotics and Automation Letters*, vol. 7, no. 3, pp. 6950–6957, 7 2022.

[37] J. Shintake, S. Rosset, B. Schubert, D. Floreano, and H. Shea, "Versatile Soft Grippers with Intrinsic Electroadhesion Based on Multifunctional Polymer Actuators," *Advanced Materials*, vol. 28, no. 2, pp. 231–238, 1 2016.

[38] J. Shintake, B. Schubert, S. Rosset, H. Shea, and D. Floreano, "Variable stiffness actuator for soft robotics using dielectric elastomer and low-melting-point alloy," in *2015 IEEE/RSJ International Conference on Intelligent Robots and Systems (IROS)*, Sep. 2015, pp. 1097–1102.

[39] D. J. Levine, K. T. Turner, and J. H. Pikul, "Materials with Electroprogrammable Stiffness," *Advanced Materials*, vol. 33, no. 35, p. 2007952, 2021. [Online]. Available: https://onlinelibrary.wiley.com/doi/abs/10.1002/adma.202007952

[40] B. Holschuh, E. Obropta, L. Buechley, and D. Newman, "Materials and textile architecture analyses for mechanical counter-pressure space suits using active materials," *AIAA SPACE Conference and Exposition 2012*, no. September, pp. 1–17, 2012.

[41] H. Imamura, K. Kadooka, and M. Taya, "A variable stiffness dielectric elastomer actuator based on electrostatic chucking," *Soft Matter*, vol. 13, no. 18, pp. 3440–3448, 2017, publisher: Royal Society of Chemistry.

[42] T. S. Krüger, O. Çabuk, and J. Maas, "Manufacturing Process for Multilayer Dielectric Elastomer Transducers Based on Sheet-to-Sheet Lamination and Contactless Electrode Application," *Actuators*, vol. 12, no. 3, p. 95, 2 2023.

[43] T. A. Gisby, B. O'Brien, S. Q. Xie, E. P. Calius, and I. A. Anderson, "Closed loop control of dielectric elastomer actuators based on self-sensing displacement feedback," *Smart Materials and Structures*, vol. 25, no. 3, p. 797620, 2011. [Online]. Available: http://proceedings.spiedigitallibrary.org/proceeding.aspx?doi=10.1117/12.880711

[44] Z. Suo, "Theory of dielectric elastomers," *Acta Mechanica Solida Sinica*, vol. 23, no. 6, pp. 549–578, Dec. 2010. [Online]. Available: https://www.sciencedirect.com/science/article/pii/S0894916611600049

[45] J. Grossert and H. Schulzs, "Electrostatic screening by a plane grid in the UK," *J. Phys. D: Appl. Phys*, vol. 22, pp. 723–729, 1989. [Online]. Available: http://iopscience.iop.org/0022-3727/22/6/001

[46] J. G. Fox and J. Mahanty, "The Effective Mass of an Oscillating Spring," *American Journal of Physics*, vol. 38, no. 1, pp. 98–100, Jan. 1970. [Online]. Available: https://pubs.aip.org/ajp/article/38/1/98/1048409/The-Effective-Mass-of-an-Oscillating-Spring

Acknowledgements

Non-authors The authors would like to thank Dr. Matthias Kollosche for his assistance in the initial conceptualization of the hybrid electrodes concept and Prof. YuFeng Chen for providing us with many best practices for fabrication of CNT-based electrodes.

Funding This material is based upon work supported by, or in part by, the US Army Research Office (award number W911NF2210219) and the National Science Foundation (award number DMR-2011754). Any opinions, findings, and conclusions or recommendations expressed in this material are those of the authors and do not necessarily reflect the views of the Army Research Office or the National Science Foundation.

Author contributions A.J.C. conceived of hybrid concept; developed vacuum filtration BSS concept; developed and implemented adaptive pre-clearing algorithm; created RC analysis code; prepared, tested, and analyzed breakdown and resistance test samples; prepared figures; and drafted and edited manuscript. M.C.Y. fabricated vacuum filtration setup; performed and analyzed cyclic testing; prepared videos; assisted with fabrication and characterization of actuators; and extensively edited manuscript. M.C. fabricated, tested, and analyzed data from "artificial muscle" actuators; and edited manuscript. S.X. fabricated, tested, and analyzed data from roll actuators; and edited manuscript. R.J.W. assisted with hybrid electrode and adaptive pre-clearing conceptualization; manuscript and figure outlining; and extensive figure and manuscript review.

List of Supporting Information for

Hybrid electrodes resolve the breakdown-conductivity tradeoff in dielectric elastomer actuator multilayers

Supporting Information
Figs. S1 - S17
Tables S1 - S2
Descriptions for Movies S1 - S3
References for Supporting Information

A Supporting information

A.1 Pre-clearing logic and hardware

The pre-clearing algorithm is split across host and target computers, and the command and feedback signals are routed through a DAQ and high voltage amplifier, as noted in Fig. S1. The host computer's logic, executed after each episode, is fully enumerated in Fig. S2.

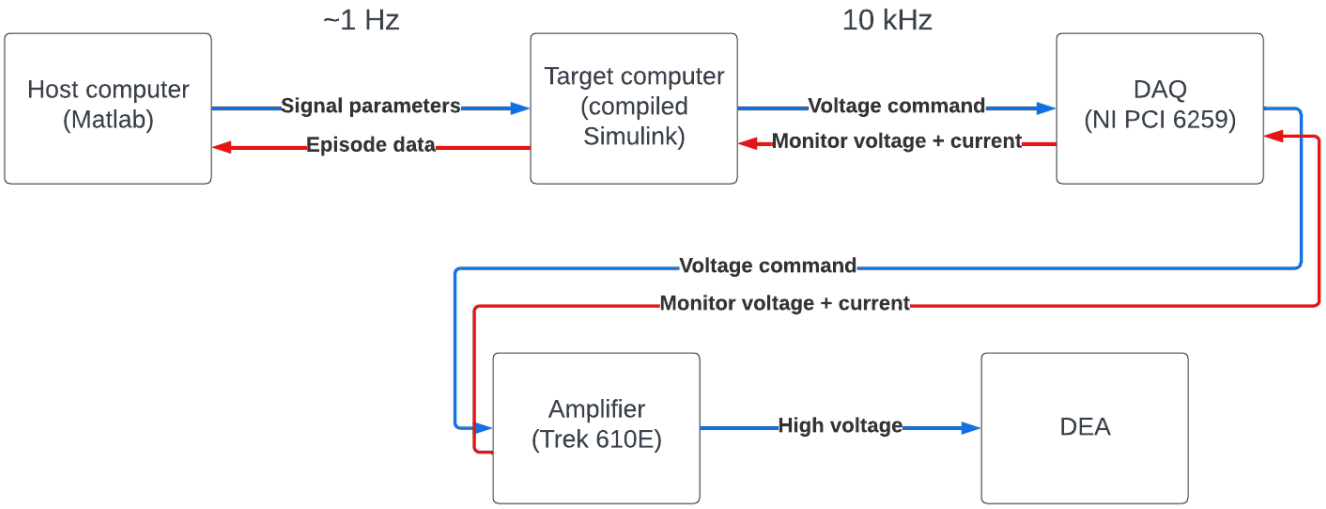

Figure S1: Signal diagram of the hardware on which the pre-clearing algorithm is deployed. Communications between the host, target, and DAQ are digital, while signals sent between the DAQ, amplifier, and DEA are analog.

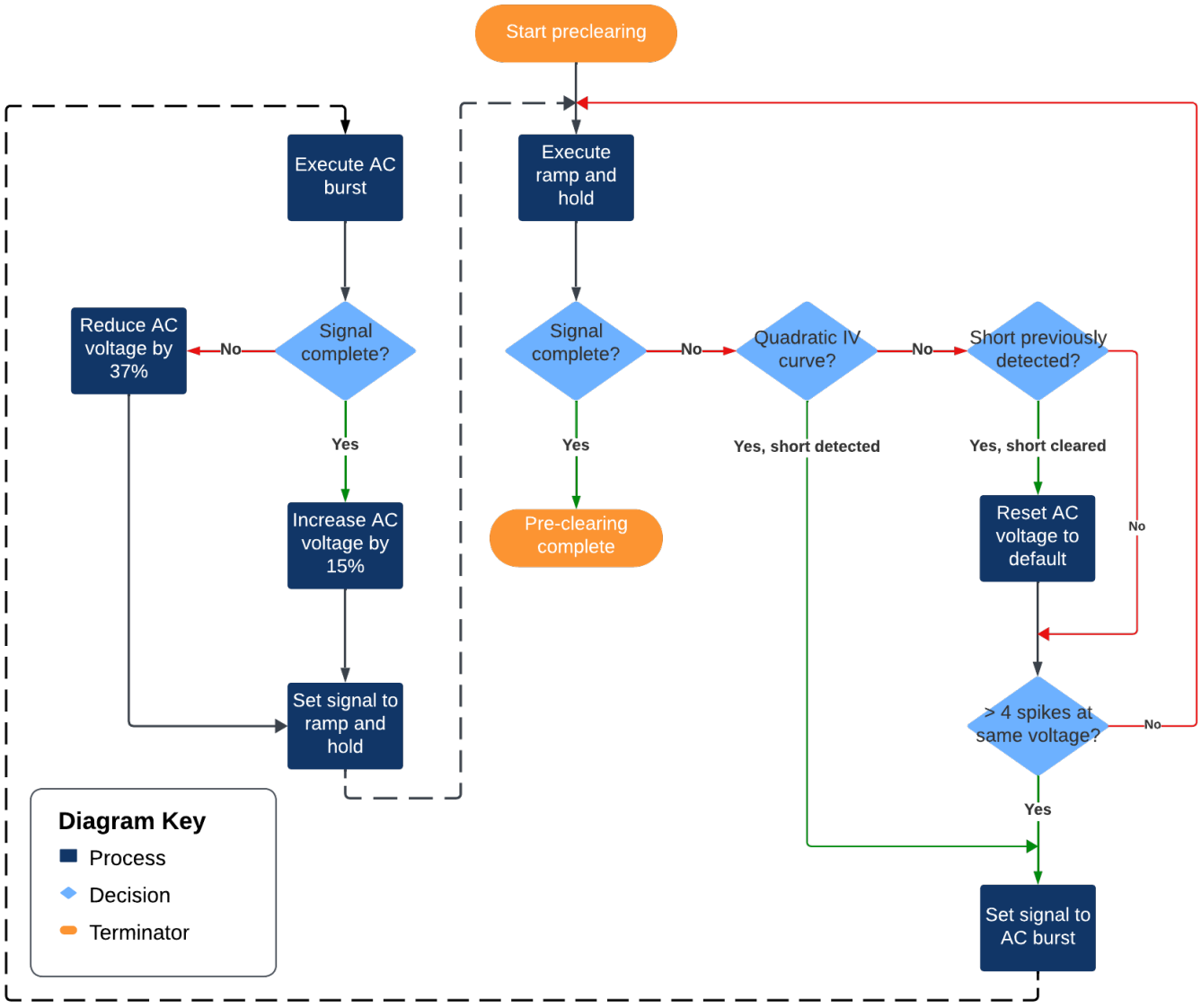

Figure S2: Overview of the pre-clearing algorithm. Dashed lines indicate a change in pre-clearing strategy. A complete signal indicates that no over-current events have occurred during the episode associated with it.

A.2 Pre-clearing effect on device resistance

During pre-clearing, devices experience thousands of actuation cycles as a result of AC bursts and ramp-and-hold episodes used to clear defects. Throughout this process, however, there is not a noticeable increase in device resistance, which encompasses both the resistance of the contacts and the electrode body. Fig. S3 shows that after preclearing to 7.8 V/µm (250 V) to eliminate initial short-circuits in the as-manufactured devices, the mean resistance of single-layer encapsulated paddle DEAs was 269$k\Omega$. Continuing the pre-clearing process up to the target of 47.0 V/µm (1500 V) resulted in a mean resistance of 265$k\Omega$. This indicates that, despite the thousands of actuation cycles, there was little damage incurred in either the body or contacts of the electrode.

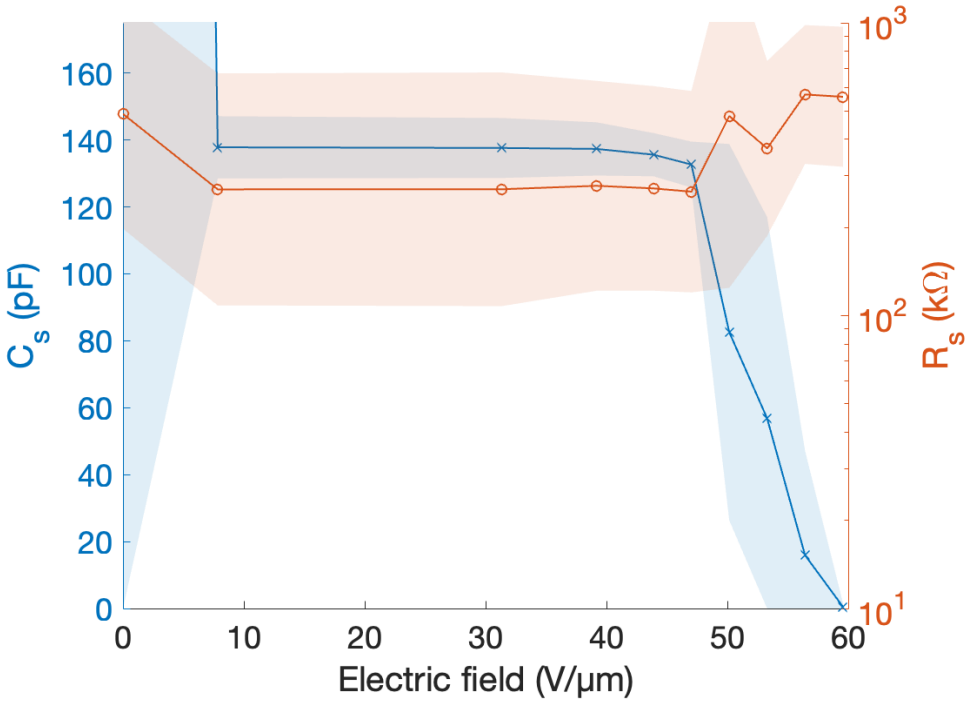

Figure S3: Total series capacitance C_s and resistance R_s as a function of preclearing voltage reached for n=10 DEAs. Shaded bounds represent $\pm 1SD$ and $\pm 1SD_{log}$ from the mean of C_s and R_s, respectively.

A.3 DEA circuit modeling

We model our DEA as a simple series RC circuit, which acts as a low-pass filter. Other circuit models have incorporated a resistor in parallel with C to model the leakage current through the dielectric (typically on the order of nA) [43], but such a large resistance is difficult to measure and as Figure S4 demonstrates, our model behaves similarly to a real DEA without this inclusion. Below f_c, the measured capacitance of the DEA deviates from that of the equivalent series RC circuit's by less than 2%, and resistance deviates by less than 3%. Above the cutoff frequency, the measured resistances diverge, but the actuator will not be effective at frequencies above f_c and will thus not be operated in that regime.

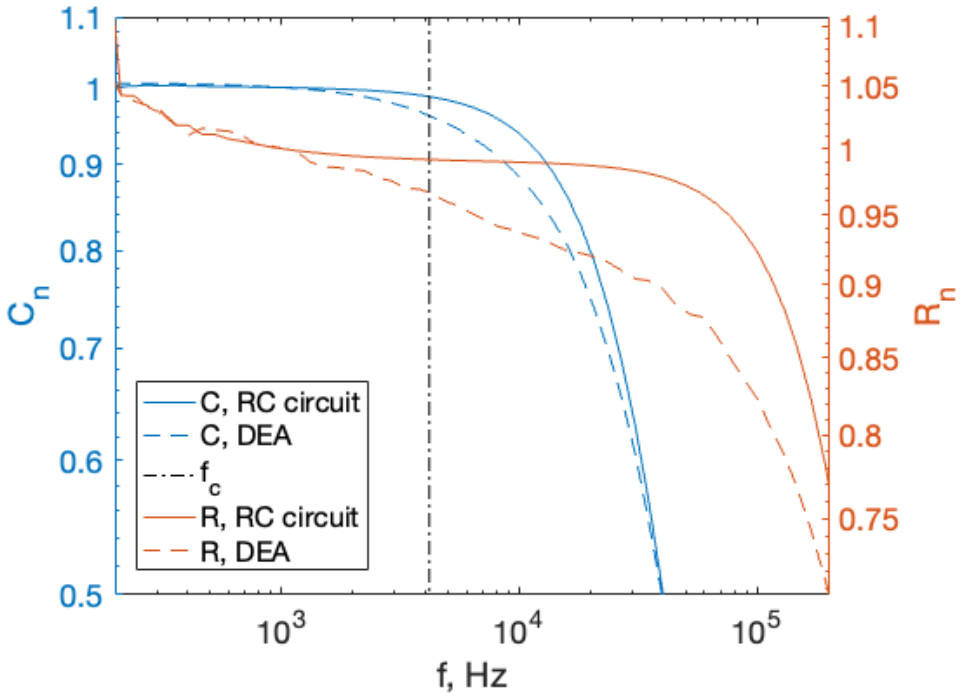

Figure S4: Comparison of resistance and capacitance measurements made with an LCR meter on a DEA and its equivalent RC circuit. Plotted values C_n and R_n are normalized by their reference values R and C measured at 1000 Hz. For the RC circuit, $R = 270.5$ kΩ and $C = 137.7$ pF and for the DEA $R = 270.2$ kΩ and $C = 137.6$ pF. The cutoff frequency f_c is calculated according to Eqn. (3) from DEA reference values.

A.4 Contact resistance measurement

Contact resistance was measured by producing 5 mm wide test strip electrodes at various lengths. Hybrid and CNT-only electrodes were sprayed using the same process described previously, with the location of different test strip lengths distributed randomly throughout the spray area. These electrodes were stamped onto $\approx$ 100 μm thick P7670 that had been spin-coated and cured onto aluminized Mylar tacked onto laser-cut acrylic disks. The aluminized Mylar was etched with a CO_2 laser cutter, leaving conductive regions at the ends of the test electrodes to serve as probe pads. After stamping, the electrodes were encapsulated with another spin-coated layer of elastomer. An X-Acto blade was then used to slice through opposite ends of the test strips to produce strips of lengths from 10 to 75 mm. After the excess silicone was removed, Pelco colloidal graphite was used to create the electrical connection between the exposed electrode and the probe pad. After the conductive paint had dried, a digital multimeter (Fluke 179) was used to measure the resistance of each strip. The resistance taken for a single test strip was the average of ten samples, as reported by the multimeter. Resistance was plotted as a function of length as shown in Fig. S5, and a linear fit was applied to the data. The contact resistance was taken to be the y-intercept of the trend line, and its confidence bound is taken to be that of the intercept. The fit of composite samples shown in Fig S5A had an $R^2 = .774$, and the 95% CI of the intercept (R_c) is [5.168, 12.47]. The fit of CNT-only samples is much worse ($R^2 = .0708$), indicating little correlation of resistance with length. This is likely due to wide variability in CNT contact resistance. The 95% CI of the intercept (R_c) is [133.5, 436.2].

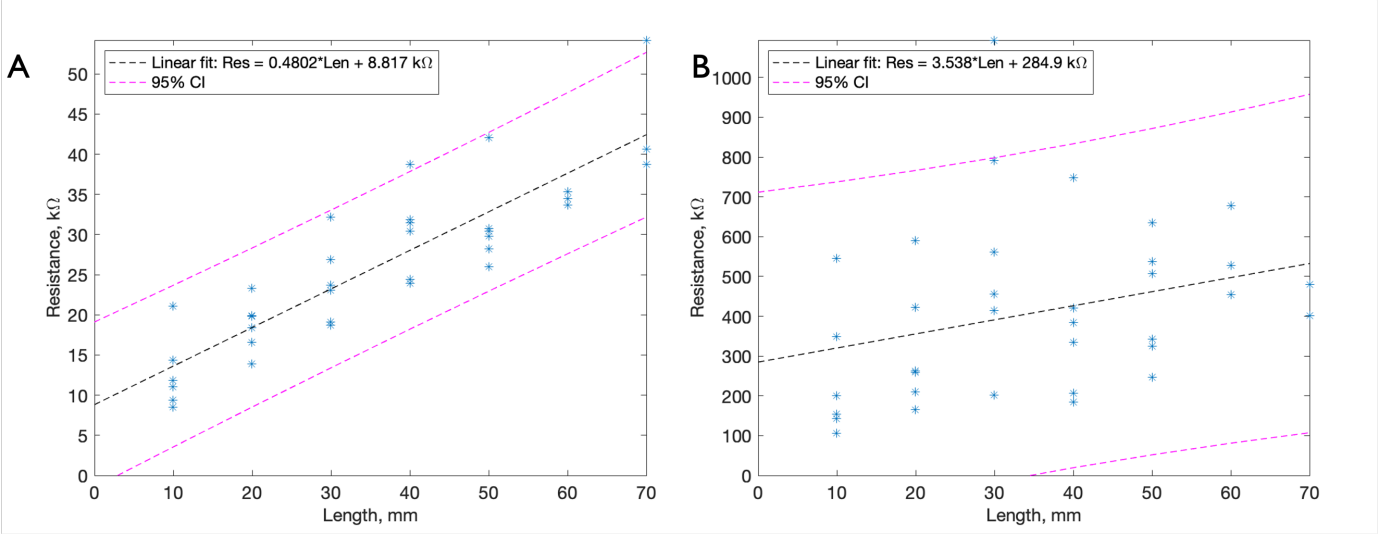

Figure S5: Total resistance vs length of 5 mm wide test strips of A) CB+CNT composite samples and B) CNT-onlysamples. The contact resistance is taken as the intercept of the linear fit, and 95% confidence interval bounds are plotted.

A.5 Cyclic testing

A.5.1 Cyclic stress-strain testing

Fig. S6 shows additional representative datasets characterizing the stress-strain behavior over 100 cycles for specimens of silicone-only and silicone-encapsulated electrodes. Each of the two layers of silicone in both samples were spin-coated for 60s at 1500rpm on an acrylic platter then allowed to cure, before stamping (if necessary) and the next layer of silicone deposition. The presence of CNTs results in a 6% stiffer specimen compared to the silicone-only samples.

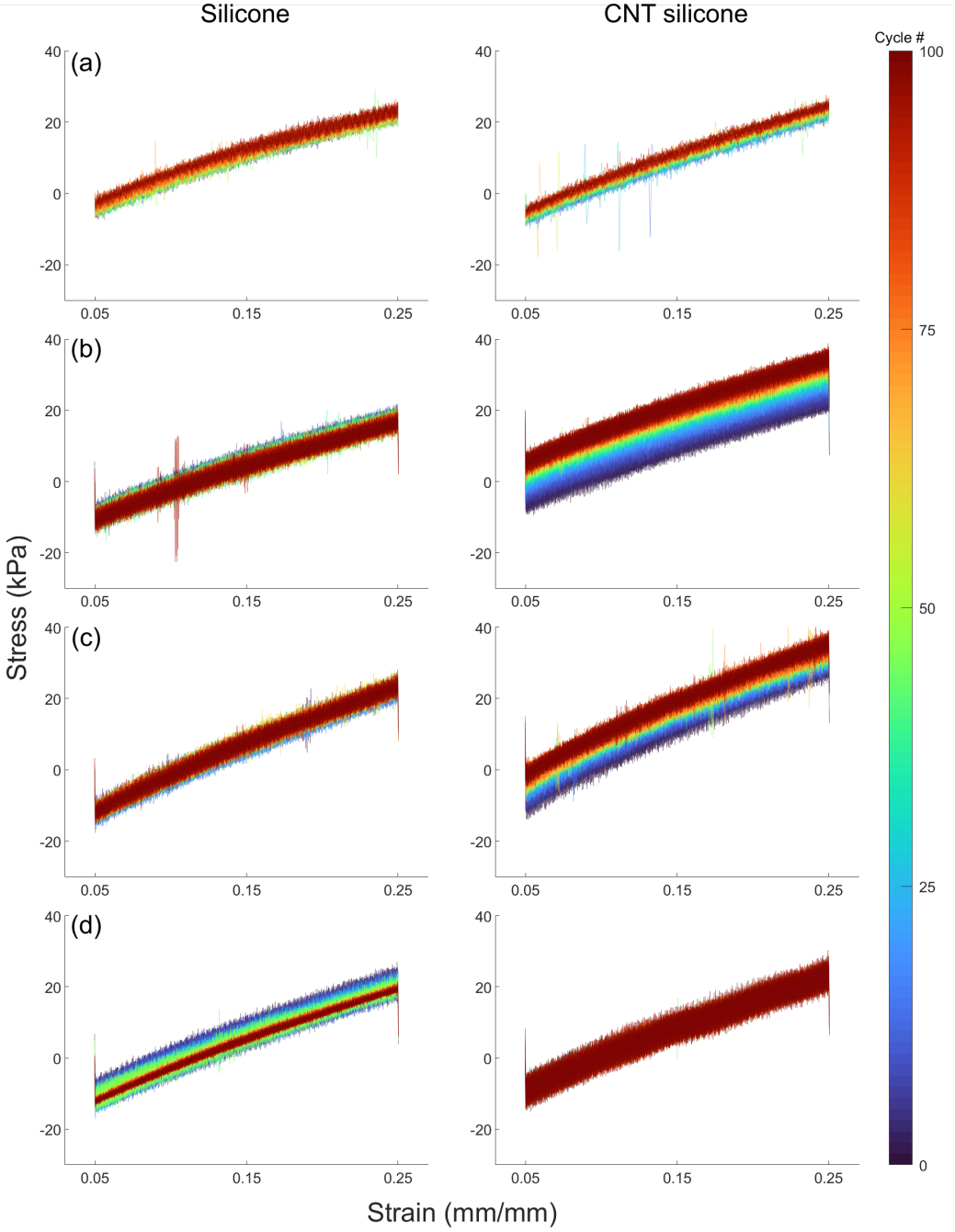

Figure S6: Stress as a function of strain over 100 cycles for all tested silicone-only and CNT+silicone samples.

A.5.2 Cyclic resistance tests

Fig. S7 and S8 show additional representative datasets characterizing the resistance-strain behavior over 100 cycles of strain to 20% and 100% for silicone-encapsulated electrodes. The samples were fabricated as discussed previously. All specimens subjected to strain cycles from 5% to 25% showed a decrease in resistance with more cycles applied (Fig. S7). For larger strains, from 5% to 105%, the behavior was less consistent, with specimens exhibiting increasing, decreasing, and no change in their resistance to strain curve (Fig. S8). With these two sets of results, we can see that the resistance evolves beneficially (higher cutoff frequency, less resistive losses) when a device is subjected to strains up to 20%. When subjected to larger strains, the electrodes can increase in resistance deleteriously, but, importantly, the electrodes retain their nominal resistance values within an order of magnitude.

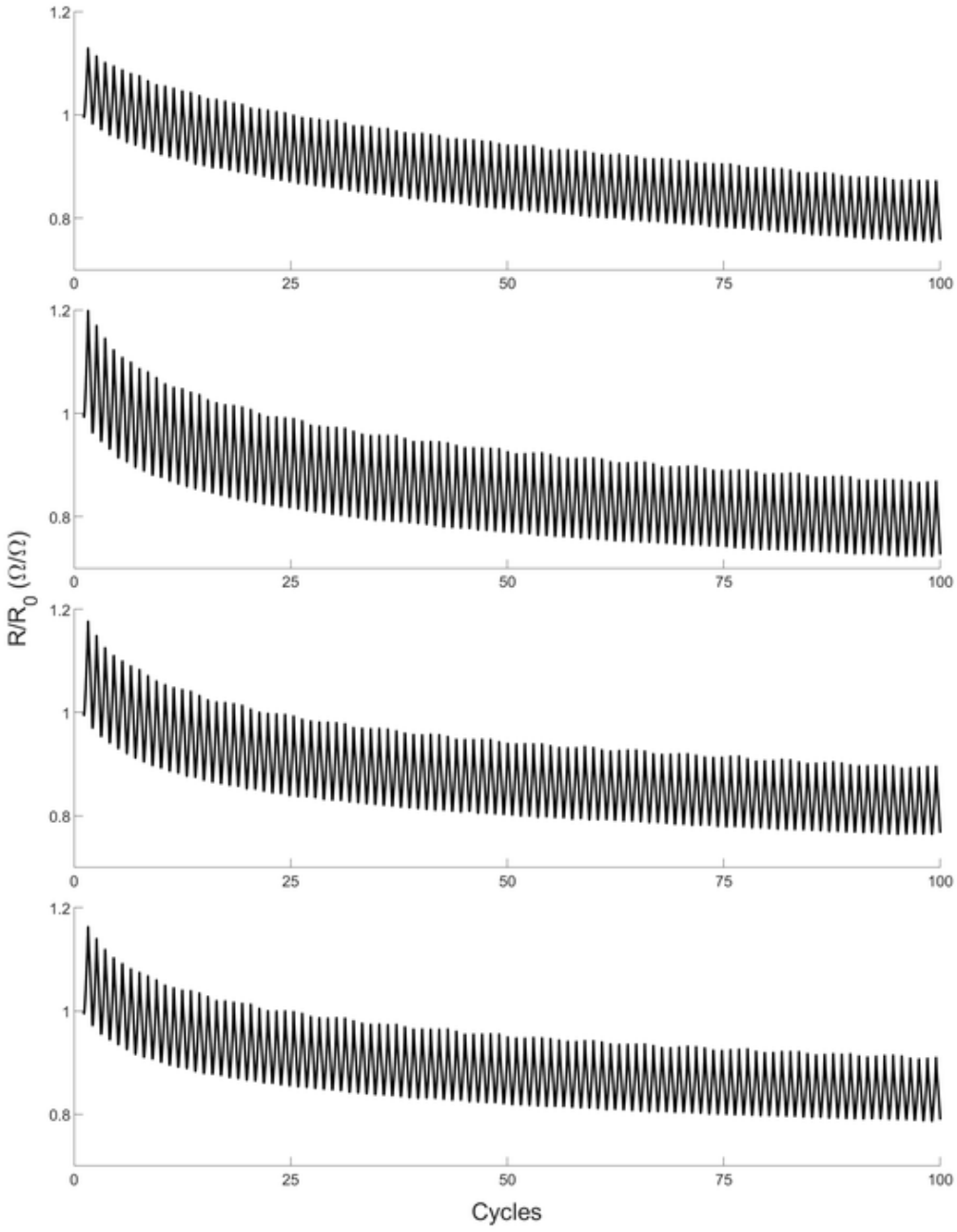

Figure S7: Resistance over 100 cycles of 5-25% strain for all tested samples

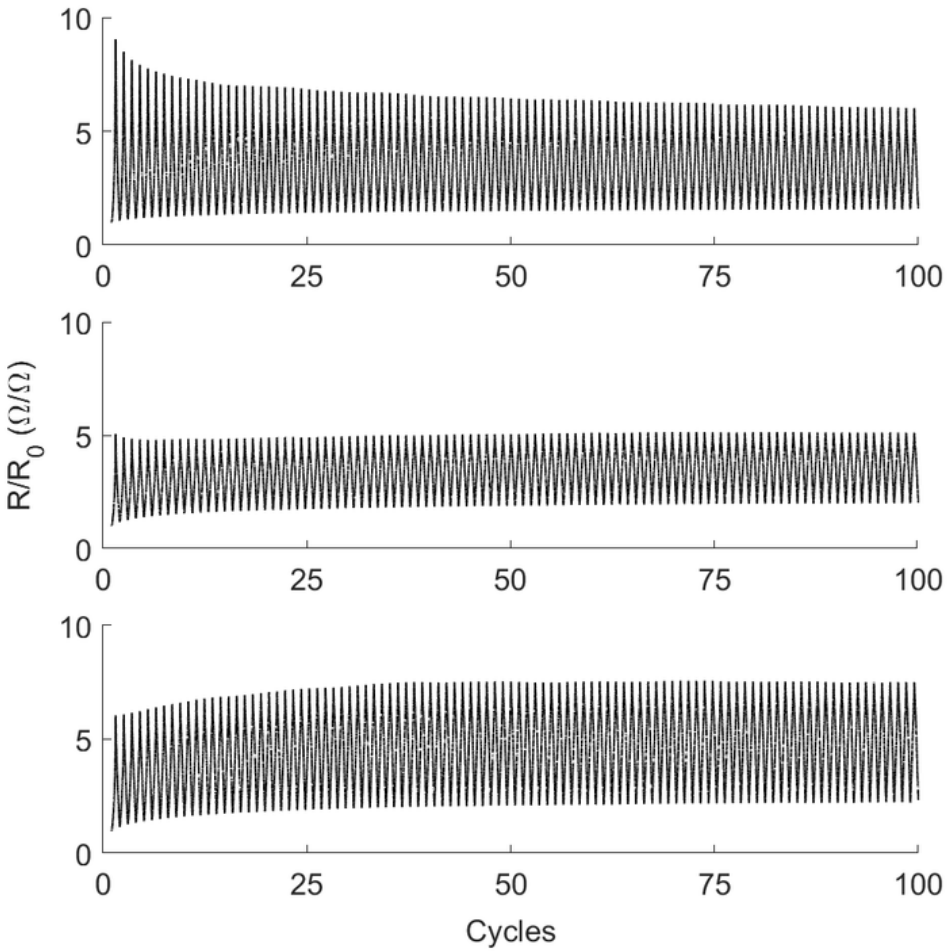

Figure S8: Resistance over 100 cycles of 5-105% strain for all tested samples

A.6 Calculation of log-space error bounds

For results displayed in log-space (Fig. 5B-D), the data were fit to log-normal distributions. While most resistance values clustered around the median, a few were much higher, likely due to manufacturing defects and inhomogeneities. Since dissipation factor and cutoff frequency are products of resistance, they display a similar distribution. Log-normal distributions better fit these asymmetric data than normal distributions do. Error bounds for the data were thus calculated by fitting to log-normal distributions in log-space, calculating the mean and standard deviation (SD_{log}), and then transforming these values back into linear space.

A.7 Fabrication process

An overview of the fabrication process is presented in Fig S9, and the mini-stack assembly process is detailed in Fig

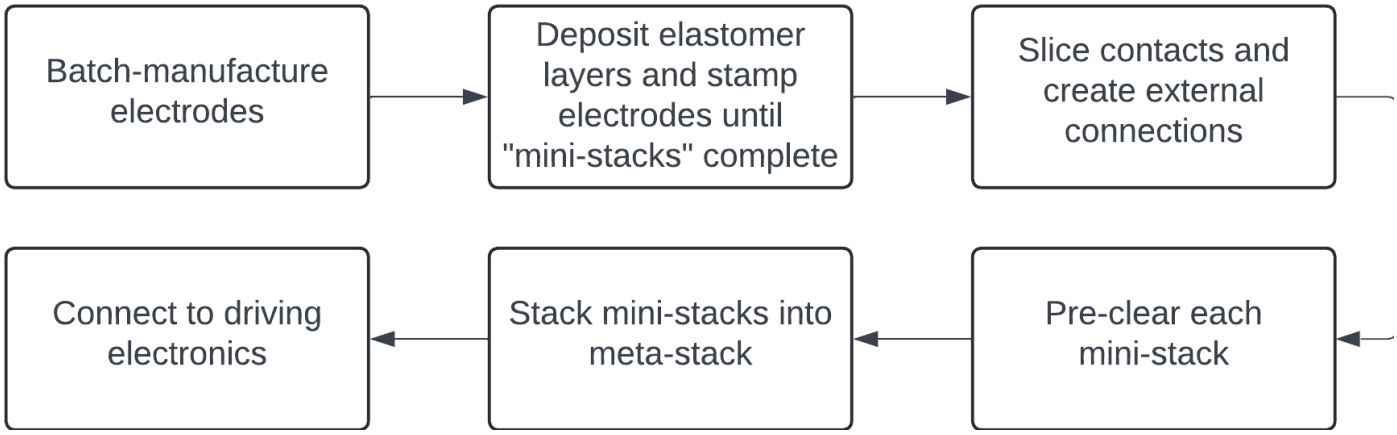

Figure S9: Overview of the DEAM fabrication process

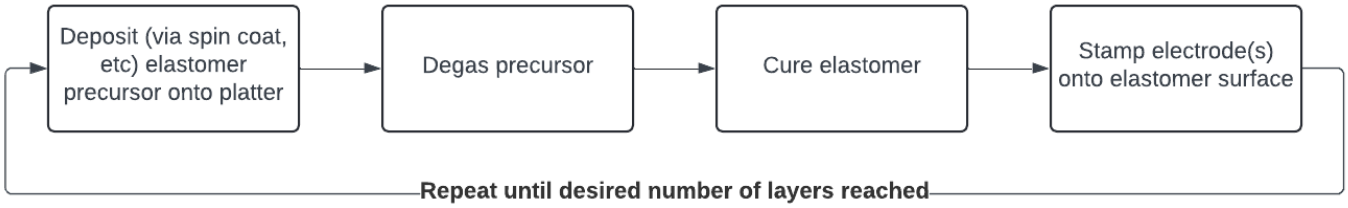

Figure S10: Mini-stack assembly process

A.7.1 Electrode deposition process

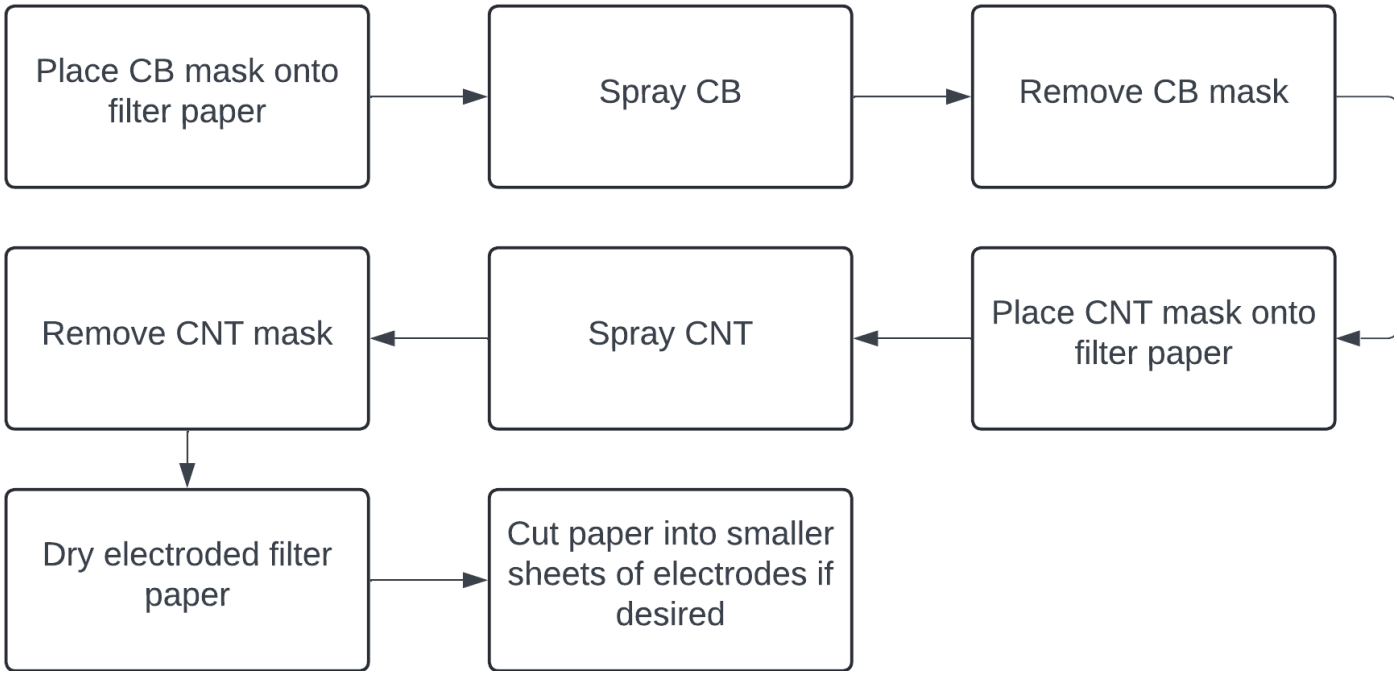

Figure S11: Summary of electrode deposition process

The CB and CNT inks are first prepared according to the processes described in Section A.7.2. Then, the inks are deposited onto the 220mm x 220mm filter paper (PTFE Membrane Stock, 45 μm pore size, Tisch). A vacuum is applied via a vacuum plate machined from porous aluminum (Metapor BF100 AL, CMT Materials). The CB ink is deposited first, and the CNT ink second. Masks, filter paper sheets, and the vacuum plate underneath are aligned with pins and corresponding holes during electrode deposition; this alignment pin system is also used for aligning the carrier substrate while stamping the electrodes onto the elastomer. For each ink, the following process is used, differing where noted:

1. Set nozzle height. The distance between the spray nozzle and the filter paper is 10cm.
2. Place filter paper on vacuum plate with four 1.5mm alignment pins, one in each corner, to fix the position.
3. Spray mixture of equal parts IPA and water onto the filter paper, ensuring the entire surface is completely wetted.
4. Place laser-cut mask (0.005" Dura-Lar Ultra-Clear Film, Grafix) over the damp filter paper, using the same four alignment pins.
5. CNT only: turn on the atomizer (SONOZAP 130kHz Atomizer, Sonaer), set to 75% power.
6. Turn on air supply.
   (a) For CB, set to 2 psi.
   (b) For CNT, set the CNT air supply to 2.5 psi, and the pro-wetting (IPA) air supply to 8 psi. The IPA pro-wetting is used to keep the filter paper wetted and enhances the uniformity of deposited CNTs.
7. Turn on the pump(s).
   (a) For CB, set the peristaltic pump (Braintree Scientific) to 6mL/min, and do not turn on the IPA syringe pump.
   (b) For CNT, set the syringe pump (Braintree Scientific) to 2.5mL/min, and the IPA syringe pump to 3.5 mL/min.
8. Turn on the vacuum.
9. Shut the gantry door.
10. Once the ink dispensing has equilibrated, begin the corresponding G-code for spraying CB or CNT. Here, the ink was deposited on the entire 220×220 mm mask area with a raster pattern sweeping over the surface of the filter paper at a feed rate of 2000 mm/min.

11. When spraying has finished, turn off all pumps, turn off vacuum, remove and discard the mask, and place the filter paper in the oven at 50°C for 5 minutes or allow to dry at room temperature for ≈1 hour.

A.7.2 Electrode ink recipe

The following recipe is used to prepare CB and CNT inks immediately before spraying (to avoid particle sedimentation). The recipes for the stock inks used can be found in Sections A.7.3 and A.7.4.

CNT ink

1. By volume, mix one part stock CNT ink with two parts IPA (approximately 15 mL of this spray ink mixture is needed for each sheet of electrodes) in scintillation vial(s).
2. Bath sonicate (CO-Z Ultrasonic Cleaner) for 30 minutes.
3. Load ink into a syringe, and place syringe into syringe pump.

The IPA cosolvent in the CNT spray ink allows it to wet the hydrophobic filter paper.

CB ink

1. Re-sonicate the stock CB ink for 10 minutes at 75% power, 100% duty cycle with a tip sonicator (QSonica Q500, 1/2" tip). Use an ice bath to prevent overheating.
2. Before particles can settle out of solution (∼30 min), extract required amount of stock ink into a disposable cup and dilute by volume with IPA at 1:9 ratio. Approximately 50 mL of CB spray ink is needed for each electrode sheet.
3. Place a stir bar in mixture and place cup onto magnetic stir plate in spray gantry. Insert feed tube for peristaltic pump.

A.7.3 CNT stock ink recipe

The following recipe is used to prepare the stock CNT ink used for spraying:

1. Add 100 g of de-ionized (DI) water to 100 mg of CNT powder (P3 SWCNT, Carbon Solutions) in a glass bottle.
2. Tip-sonicate (QSonica Q500, 1/2" tip) the solution for 30 minutes at 75% power with 30 sec on, 10 sec off duty cycle (40 minutes elapsed). Use an ice bath to prevent overheating.
3. Centrifuge (Biofuge Primo, Sorvall) the mixture at 8100 RPM for 60 min in 50 mL Falcon tubes.
4. Extract the supernatant, leaving the bottom 5 mL.
5. Determine the relative concentration of the ink compared to a 17% transmittance sample. Place 0.5 mL of the ink in a scintillation vial and successively dilute with DI water, measuring transmittance starting at 8× dilution and continuing gathering measurements every 2-4× until a transmittance of over 17% is reached. Use linear regression to find the current dilution ratio, D_{init}, for 17% transmittance.
6. Dilute the ink to 16× relative concentration. Add DI water with volume = $(\frac{D_{init}}{16x} - 1) \times V_{init}$, where V_{init} is the original volume of ink with D_{init}x concentration.

The determination of relative concentration accounts for variation in the measurement of DI water and CNT powder, sonication, and centrifugation steps.

A.7.4 CB stock ink recipe

The following recipe is used to prepare the stock CB ink used for spraying:

1. Add 80 g IPA to 800 mg CB (Printex XEB2, Orion Engineered Carbons)
2. Tip-sonicate (QSonica Q500, 1/2" tip) for 30 minutes at 75% power, 100% duty cycle. Use an ice bath to prevent overheating.

A.7.5 External connections

Figures S12 and S13 show the process of connecting the electrodes to external electronics. First, a vertical cut is made through the layers. This exposes the cross-section of the nanoparticles. Next, a colloidal graphite paint is applied to the cross-section and extended to nearby copper leads.

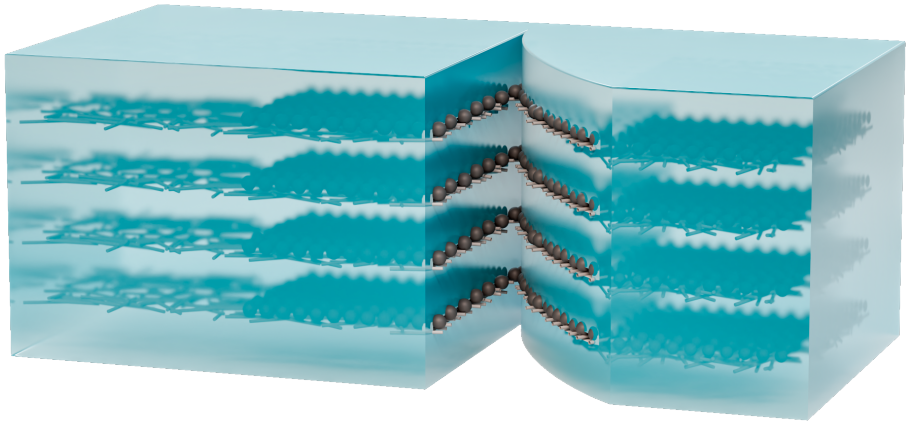

Figure S12: A cut is made into the multilayer, exposing the nanoparticle cross-sections. The excess multilayer is peeled away and discarded.

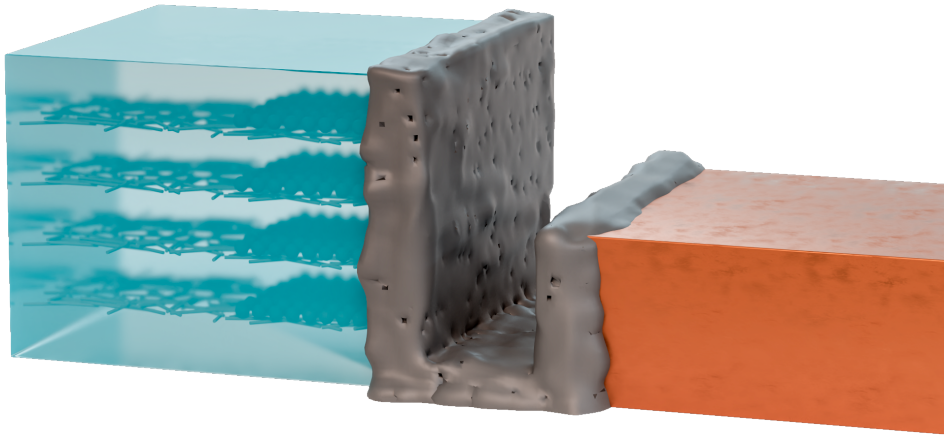

Figure S13: A colloidal graphite paint is applied to the exposed cross-section and nearby copper leads. This creates the electrical connection between DEAM electrodes and the external power supply.

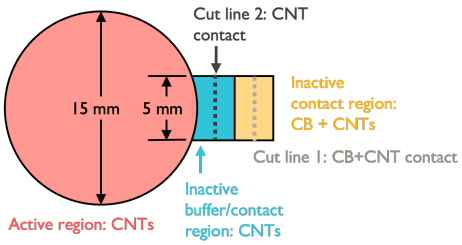

Figure S14: Diagram of the paddle electrodes used to test the effect of CB+CNT vs CNT-only regions at the contacts on total device resistance. LCR data was first taken from connections made by slicing at the first cut line, within the CB+CNT region. The cut and connection was remade along a second line within the CNT-only region.

A.8 Cost estimate

Tables S1 and S2 summarize the differences in material cost to produce an actuator with hybrid electrodes via the presented batch spray and stamp process ($22.22) vs that to produce a CNT-only actuator with the mask-and-stamp process utilized in [24] ($273.87). The reference point used is an artificial muscle of the same design as presented in this work (100 15-mm-diameter active layers, each 85 µm thick).

The main driver of cost for both actuators is the filter substrate. While the Advantec filters can theoretically be reused, their performance quickly degrades with reuse, and thus in [24] each filter was used to produce only a single electrode layer. For cost purposes they are thus treated as disposable, and account for 86% ($236.54) of the total cost. This calculation also assumes that 20 10×10 mm electrode layers can pack into an 80 mm diameter usable area of the filters, a relatively ideal assumption because of practical handling limitations. The Tisch filter paper, however, is an order of magnitude cheaper, costing $12.56 for the same area. Additionally, our CNT ink based on P3 CNTs (Carbon Solutions) is far more cost effective than the Invisicon 1210 ink from Nano-C, lowering the CNT cost from $30.00 to $3.36.

Costs could be further reduced by increasing the areal density of stamp electrodes in a given sheet. Currently, only 48 paddle electrodes are patterned onto each sheet for ease of handling, but a simple rectangular pattern of the paddle electrodes with 20 mm spacing would allow for 121 electrodes on a single sheet. Such an increase would proportionally decrease the major drivers of cost: PET for masks, filter paper for electrode stamps, and CNTs for the ink.

Component	**Purchase Price ($)**	**Purchase quantity**	**Unit**	**Quantity per actuator (100 layers)**	**Cost per actuator ($)**
Wacker P7670	2250	50000	g	72	3.24
IPA	34	5000	mL	100	0.68
CNT ink	2000	200	mg	3.00	30.00
Advantec filters	295.68	25	each	20	236.54
Silicone release film (mask)	350	3.17E+07	mm^2	2.00E+05	2.21
VHB film (mask backing)	100	1.67E+07	mm^2	2.00E+05	1.20
				TOTAL	273.87

Table S1: Accounting of the costs of the mask-and-stamp process described in [24].

Component	**Purchase Price ($)**	**Purchase quantity**	**Unit**	**Quantity per actuator (100 layers)**	**Cost per actuator ($)**
Wacker P7670	2250	50000	g	36	1.62
IPA	34	5000	mL	180	1.22
CB	20	1000	g	0.15	0.003
CNT	280	1000	mg	12	3.36
Tisch PTFE paper	54.60	0.9	m^2	0.207	12.56
PET	14.40	25	each sheet	6	3.46
				TOTAL	22.22

Table S2: Accounting of the costs for the batch spray and stamping of hybrid electrodes presented in this work.

A.9 Artificial muscle

A.9.1 Artificial muscle DEAM fabrication

We followed the batch-spraying and stamping process seen in [12] to create 10 10-layer DEAs which were then combined into a 100 layer DEAM that measured 10.6 mm thick. Each layer was of the same 15 mm diameter paddle-shaped design shown in Fig. 1. To make these 10-layer mini stacks, we spin-coated Elastosil P7670 onto a PET substrate loosely adhered to an acrylic base plate for rigidity during spin coating. The first and last layers were spin-coated at 1500 RPM, and the active layers were spun at 560 RPM for a thickness of 85 μm. Each stack had 11 electrodes for a total of 10 active layers. We placed a protective sheet of PET on top of the platter and then used a laser cutter (Universal Lasers VLS6.60) to release cut each mini stack, leaving a 0.5mm non-conductive buffer around the edge of each mini stack to prevent exposing the electrodes to the air, which we have observed as a cause of premature breakdown. With the mini stacks cut out but still attached to the platter, we removed the excess silicone. As described in Section A.7.5, we used a knife to make a cut to expose the carbon black connections, then connected each stack to external electrical leads using conductive ink. After pre-clearing each mini stack to 45 V/μm according to the process previously described in the main text, we measured the capacitance and discarded those that dropped under 80% of the expected capacitance from $C_{expected} = n\frac{A\epsilon}{H}$, where n is the number of active layers, A is the active area of each layer, ϵ is the permittivity of the dielectric material, and H is the distance between layers. With the remaining mini stacks, we removed the handle layer of PET from the base sheet of acrylic, removed the protective PET cover sheet, coated the exposed surface in a thin glue layer, then laid each into a laser-cut mold to align subsequent mini stacks. These intermediate meta stacks were then placed in an oven at 60° for 15 minutes, at which point the PET substrate was removed and another mini stack was added, repeating the process until all 10 mini stacks were combined into one meta stack. The glue layer was made by depositing a small pool of Elastosil onto a sheet of PET, then squeegeeing the pool into a thin film. Each resulting glue layer was on the order of 5 μm thick. To avoid possible breakdown through air bubbles trapped in the glue layer, each mini stack was aligned so there was no field between subsequent stacks. With the completed stack, we then made a cut through all layers of CB to expose a single face to connect to. We then painted the exposed CB face with conductive ink, connected the ink to an external electrical lead, and encapsulated the dried ink with a layer of silicone to prevent flaking.

A.9.2 Artificial muscle characterization

To measure free displacement for the stack actuator, we suspended the device by the leads, applied a 3100V sinusoid at 1 and 5 Hz, recorded movie at 30 fps, and measured the through-thickness strain using a custom MATLAB script. The expected strains are predicted with the voltage-stretch relation given in [44]: $V = H\lambda^{-2}\sqrt{\sigma(\lambda)/\epsilon}$, where V is the voltage across the electrodes, H is the active layer thickness, λ is the in-plane stretch, and σ and ϵ are in-plane stress and strain, respectively. The Maxwell stress calculation assumes an ideal electrode with complete coverage, but as seen in Fig. 1D, CNTs do not cover the entire area of the electrode [8,9,45]. We thus introduce C_{pe} as a metric to account for capacitance loss through fractional coverage as well as from layer misalignment and pre-clearing ablation post fabrication such that $C_{pe} = C_{re}C_{fe}$. We define this quantity as the ratio of the measured capacitance (4.6 nF) to the expected capacitance predicted by $C_{expected} = n\frac{A\epsilon}{H} = 5.3$ nF, where n is the number of layers, the area A = 1.77×10^{-4} m^2, $\epsilon = 2.61\times10^{-11}$ Fm^{-1}, and layer height $H = 85\mu$m, thus $C_{pe} = \frac{4.6nF}{5.3nF} = 0.86$. The stress is given by $\sigma(\lambda) = \mu\left(\lambda^2 - \lambda^{-4}\right) \times C_{pe}^{-1}$, where μ is the shear modulus of the elastomer. To account for the added stiffness caused by the added 14% inactive area cut around the perimeter of the electrodes and 25% inactive height from encapsulation and glue layers, a factor of 1.43 is applied to the measured shear modulus of Elastosil P7670 (53 kPa). This model predicts approximately 29% vertical (through thickness) strain at 3100V for 85 μm layers with a breakdown field of 47V/μm, above our measured average value of 19% strain over active thickness (15% strain over total thickness) at 3100V, found using the measurement process used in [12]. To perform a test to determine the frequency response of this stack, an amplifier capable of producing a current of $I = \pi fCV$ is needed, where f is the operating frequency in Hz, C is the capacitance of the stack (measured to be 4.6nF), and V is the operating voltage, 3100V in our case. Because our amplifier is only capable of generating a current of 2 mA, the maximum frequency is approximately 44 Hz. Thus, we did not perform a full frequency sweep with this device.

After measuring free displacement with minimal boundary constraints, we measured the blocked force with rigid connections on either end to minimize displacement. We used Tech-Bond (Tech-Bond Solutions) to attach the terminating faces of the actuator to 1/16" thick pieces of acrylic with embedded jewelry hooks to make these external connections. The caps were then attached via "S" hooks to a load cell on the top (Transducer Techniques MDB 2.5) and a micrometer stage on the bottom to control pre-tension. With approximately 5% pre-strain in tension, we measured a maximum actuation force of 4.5N at a field of 43 V/μm before visible delamination occurred between mini stacks. This delamination occurs at approximately 63% of the expected value of 7.2 N given by $F_{expected} = C_{pe}\epsilon E^2 A$. We suspect cure inhibition prevented strong lamination between mini stacks, as we were not able to repair the stack in such a way as to prevent further delamination, but the source of this cure inhibition is still undetermined. Because the stack maintained the measured

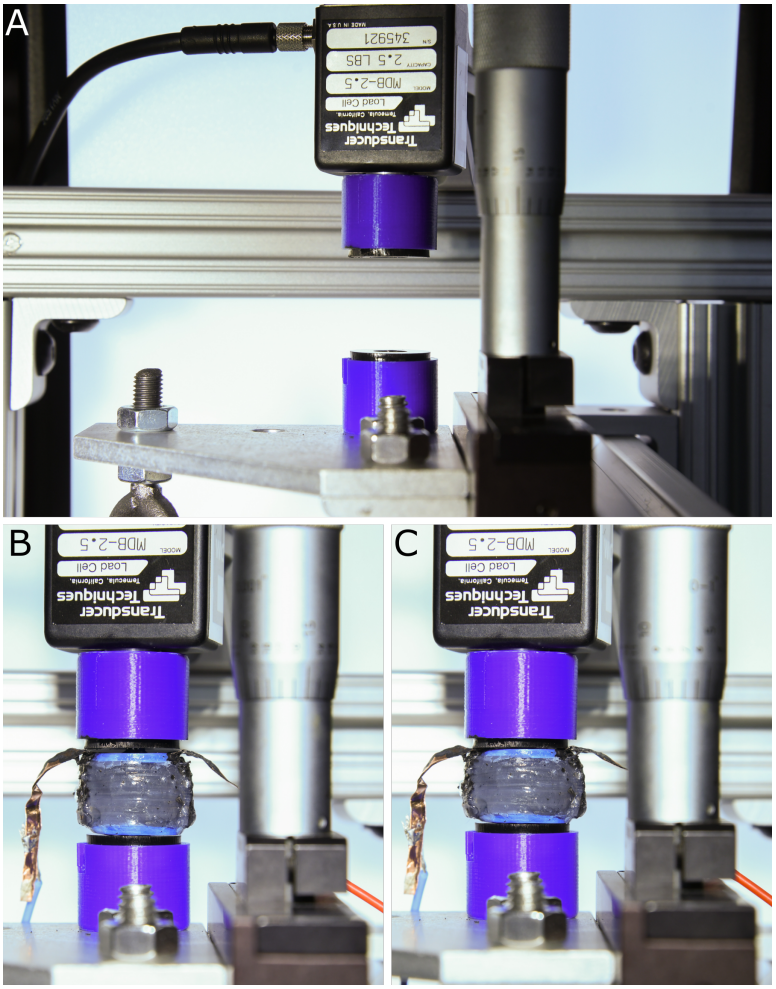

Figure S15: **Setup for measuring artificial muscle blocked force (A)** Experimental setup showing the load cell mounted rigidly at the top. A linear stage is mounted to the right which raises and lowers the bottom stage. **B** and **C** show an artificial muscle DEAM loaded into the setup in the uncompressed (relaxed) and compressed state, respectively.

capacitance value after delamination occurred, we chose to continue testing in compression so the actuation direction would match the pre-tension direction and there would be no risk of delamination. In the compression configuration, we sandwiched the stack between two acrylic plates connected to the load cell and micrometer stage. While this configuration does not represent a practical implementation for a stack actuator, it allowed us to quantify the force generated without concern for delamination. With 1.5mm (14%) pre-strain in compression and a field of 45V/μm, we achieved 6.9 N of force, 87% of the $F_{expected}$ of 8.0N at the corresponding field. During the manufacturing process, we observed minor misalignments between some stamped layers, likely due to stretched alignment pin holes on the filter paper. More careful observation and control of these alignment holes can help bring the force closer to the expected value, as well as increase C_{pe}, but it is unlikely that 100% of the expected force can be achieved due to incomplete CNT coverage.

A.10 Roll actuator

A.10.1 Roll actuator performance comparison

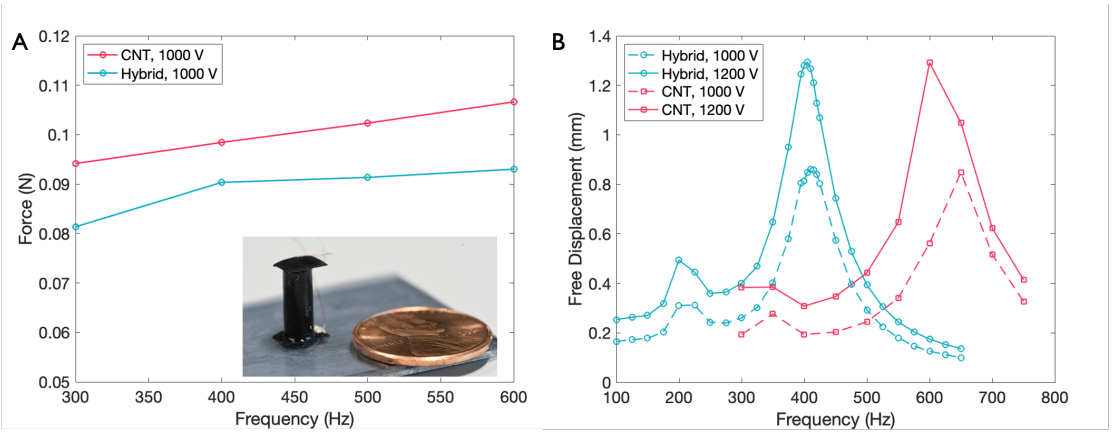

Figure S16: **Performance comparison of hybrid and CNT-only roll actuators (A)** Comparison of blocked force output vs frequency for a hybrid roll actuator, shown in inset, and an equivalent CNT-only roll actuator from previous work [24] when a 1000 V_{pp} signal was applied. **(B)** Free displacement of hybrid-electrode roll actuators vs CNT-only as a function of frequency.

A roll actuator made with hybrid electrodes achieves similar output to that from previous roll actuators made with a well-established process for stamping CNT electrodes [15, 24]. A hybrid-electrode roll actuator that has the same design parameters as those in the previous work was fabricated (Figure 6C). After pre-clearing up to 1750V, the equivalent R and C of the actuator were 25 kΩ and 1.50 nF, respectively. Based on the model we developed in [24], we expected the performance (i.e., blocked force and free displacement) of the hybrid electrode actuator to be within 10% variation from the previous devices. We experimentally measured the actuator's blocked force and free displacement as a function of operation frequency, then compared the results with those of the rolls from the previous work. The blocked force was characterized with a force sensor (Nano-17 Titanium, ATI Industrial Automation). We fixed the force sensor on a single-axis translation stage and placed the actuator under the sensor. To ensure that the actuator's motion was blocked during the test, we lowered the height of the sensor until it applied a preload of 0.005N. The actuator was operated at 1000V during the test across various frequencies, and the result is shown in Figure 6C. Compared to the previous work, the blocked force ranges from 8.2% less at 400 Hz to 13.6% less at 300 Hz. Since the actuator's electrical time constant is much shorter than the period of our applied signal, the blocked force should be independent of the frequency, but incomplete constraints on lateral motion (bulging in the center) may permit some frequency dependence of the device's mechanical behavior even in a blocked force configuration. We used a laser vibrometer (Polytec PSV-500) to characterize the actuator free displacement (Figure 6D and Supporting Movie 2). The resonance frequency of the hybrid-electrode actuator was shifted down to 400Hz compared to the previous actuators due to an increase in the height and weight of the rolls (Sec. A.10.3). However, the free displacement of the new actuator was within 1.5% of the displacement of the actuators from previous work.

A.10.2 Roll actuator fabrication

We adopted the layering and rolling fabrication method from previous works [15, 24] for the roll actuator. First, a DEA multilayer sheet is constructed. Each DEA sheet consists of six layers of CNT (Invisicon 1210, Nano-C) soft electrodes sandwiched by seven layers of dielectric elastomers (Elastosil P7670, Wacker chemie AG)242). The top and bottom encapsulation elastomer layers are spin-coated at 2500 rpm, and the functional dielectric elastomer layers are spin-coated at 1500rpm. The initial elastomer layer is thermally cured in an oven at 60°C for 30 minutes to avoid delamination from the acrylic substrate during fabrication. The rest of the elastomer layers are each cured for 15 minutes. The patterned hybrid electrodes are prepared by the spray deposition method described in the main text. The electrodes are then patterned onto the elastomer sheets with alignment pins and a roller.

After the multilayer sheet is prepared, we release cut the DEA into 11.5 mm by 54 mm samples using a programmable cutter (Silhouette America). We then roll the samples into cylinders that are 11.5 mm tall and approximately 7 mm in diameter. Lastly, two carbon fiber plates are capped to both ends of the cylinder as electrodes using carbon conductive adhesive (Engineered Materials Systems, Inc.), and wires are connected to the carbon fiber caps using silver conductive adhesive (Engineered Materials Systems, Inc).

Our hybrid electrode roll actuators are taller (11.5mm) than the previous ones (9mm) with the same active height due to an addition of the carbon black electrode. To avoid potential early breakdown induced by the carbon black electrode, a buffer zone of 1mm is needed between the carbon black electrode and the overlapped CNT electrode (the DEA active area). This buffer area is applied to both ends of the cylinder roll, which induces a height increase of 2 mm.

A.10.3 Roll actuator design changes and resonance shift

The design of a hybrid-electrode-DEA's active region remains the same as that of a previous DEA. However, a hybrid-electrode-roll-actuator (11.5 mm) is taller than previous roll DEAs of similar design (9 mm) due to the addition of carbon black into the electrode. To avoid early breakdown of the DEAs, a 1 mm tall buffer zone between the active region and the carbon black electrode region is necessary on both ends of a DEA roll. In addition, during the release cut process, it is necessary to cut into the carbon black region to expose the hybrid electrode for wiring connections. These changes increase the height and mass of the roll actuators, leading to a shift in the resonant frequency.

When characterizing the actuator's free displacement as a function of frequency, we observed the resonance of the hybrid-electrode-rolled-actuators was lower than that of previous roll DEAs with similar active areas. This result was mainly because of the geometry and mass change of the new hybrid-electrode-DEAs, which was caused by the design requirements explained above. A hybrid-electrode DEA is 11.5 mm tall and weighs 155 mg, while a previous DEA is 9mm tall and weighs 110 mg. A roll actuator's resonant frequency, ω, is a function of its stiffness, k, and mass, m ($\omega = \sqrt{\frac{k}{m}}$). The stiffness of the actuator was estimated based on the rolled actuators' length, L, cross-sectional area, A, and the modulus of the constituent elastomer, E ($k = \frac{EA}{L}$). Therefore, the resonant frequency of a rolled actuator can be determined by:

$$\omega = \sqrt{\frac{EA}{Lm}} \tag{4}$$

We defined the resonance, modulus, cross-sectional area, length, and effective mass of the hybrid-electrode-DEAs to be ω_i, E_i, A_i, L_i, and m_i, respectively, where i denotes the hybrid (1) or previous (2) design. Based on our design parameters, the modulus and cross-sectional area of the two actuators are the same, but $L_2 = 1.28L_1$. We simplified a rolled DEA to be a spring-mass system and assumed the spring has a uniform linear density. The effective mass of a DEA can then be estimated to be one-third of its total mass [46]. Together with the measurement mass of the rolled DEAs, we determined $m_2 = 1.4m_1$. Finally, based on Equation 4, we have $\omega_2 = 0.74\ \omega_1$. The measured resonance of the previous roll DEAs was approximately 600 Hz. Based on our model, the resonance peak for hybrid-electrode-DEAs is estimated to be 444 Hz, which is very close (10% higher) to our experimental result (400 Hz).

A.10.4 Roll actuator blocked force estimation

The electrical properties of the roll are described with a RC circuit, consisting of a capacitor and a resistor in series. The drive voltage to a DEA, $V_c(t)$, is given by:

$$V_c(t) = \frac{1}{2}\alpha V_{in}\cos(\omega t + \phi) + \frac{1}{2}V_{in} \tag{5}$$

and the current through the circuit is:

$$i_c(t) = -\frac{1}{2}V_{in}\alpha\omega C \cdot \sin(\omega t + \phi) \tag{6}$$

where V_{in} is the amplitude of the signal, ω is the angular frequency, and ϕ is the phase shift. The amplitude coefficient $\alpha = \frac{1}{\sqrt{(1+(RC\omega)^2)}}$ and the phase shift $\phi = tan^{-1}$(-RCω).

When a voltage input is applied, the Maxwell stress generated across the electrodes is:

$$\begin{aligned} P &= \frac{1}{2}\epsilon_p E^2 \\ &= \frac{1}{2}\epsilon_e \left(\frac{V}{d}\right)^2 \end{aligned} \tag{7}$$

where P is the Maxwell stress, E is the electric field, V is the voltage across the electrodes, ϵ_e is the dielectric constant of the elastomer, and d is the dielectric elastomer thickness. Based on our previous work [24], the blocked force of a DEA is estimated as follows:

$$F_d(t) = \frac{1}{2}\epsilon_e \left(\frac{V_c(t)}{d}\right)^2 S \tag{8}$$

where S is the cross-sectional area of the actuator. Substituting $V_c(t)$ into Equation (5), we estimate the driving force to be:

$$F_d(t) = \frac{1}{8}\frac{\epsilon_e}{d^2}V_{in}^2\left[\frac{1}{2}\alpha^2 + 1 + \frac{1}{2}\alpha^2\cos(2\omega t + 2(\phi) + 2\alpha\cos(\omega t + \phi)\right]S \tag{9}$$

A.11 SEM images of electrodes

We imaged our electrodes with a scanning electron microscope (Zeiss Gemini 360 FE-SEM) using the in-lens detector at 0.5kV accelerating voltage. The hybrid CNT/CB electrodes were sprayed onto the filter paper (PTFE Membrane Stock, 45 μm pore size, Tisch) and allowed to dry in a low-humidity box. A portion of the sprayed filter paper was then cut and adhered to the stub with carbon tape. The CNT/CB electrode was electrically grounded by painting colloidal graphite (Ted Pella) from the electrode to the stub. As seen in the image, the CNT particles conform well on and around the carbon black particles, making good electrical contact between the two types of conductive particles.

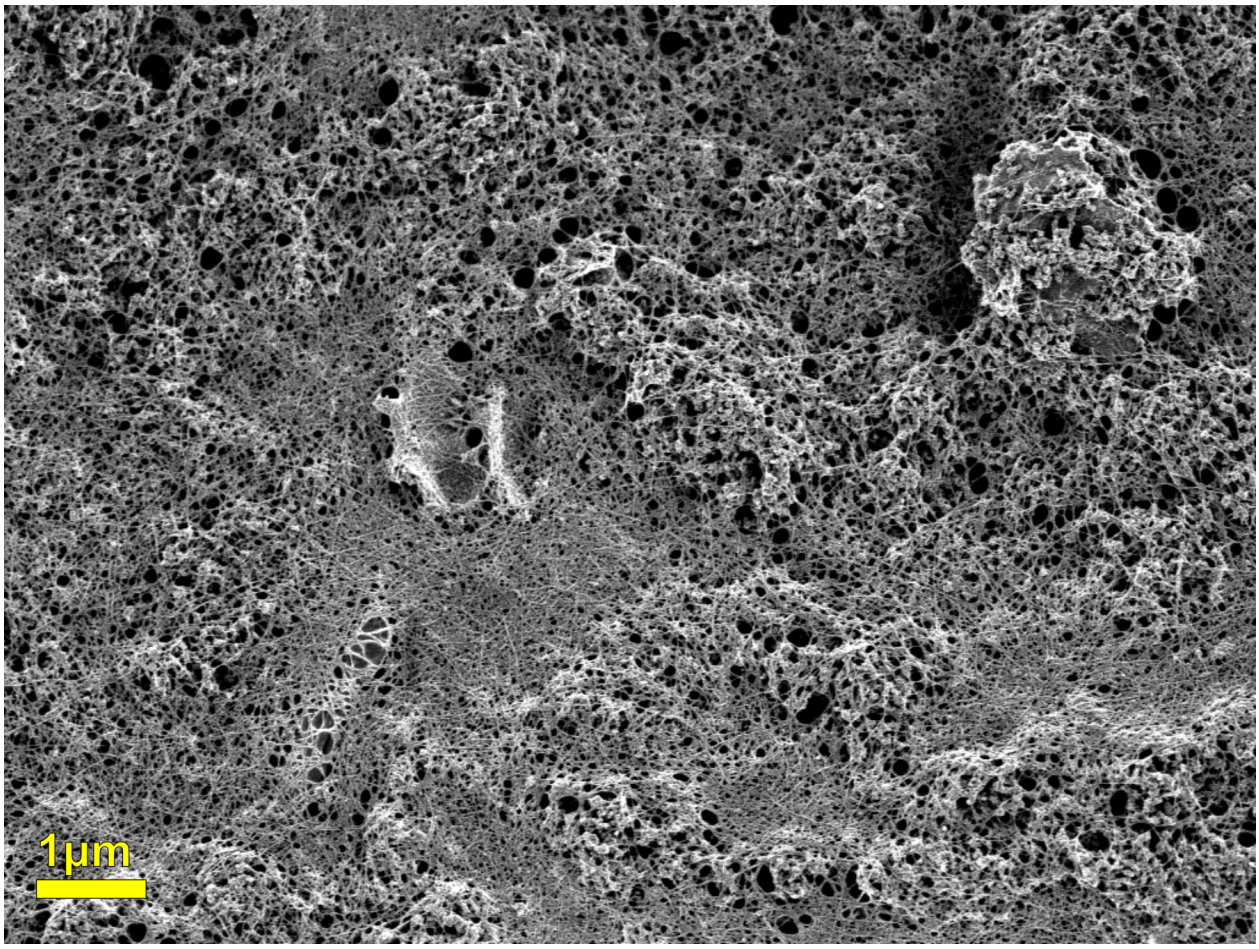

Figure S17: SEM image showing the draping of CNT particles on larger CB agglomerates after spraying onto filter paper.

A.12 Movie descriptions

Movie S1. High-speed video of pre-clearing events. Recorded at 30,000 fps with a Phantom V2512, the video is played back at 1/1000× speed. A voltage of 1500 V is applied during a pre-clearing process in which the current shutoff is not employed. Multiple flashes, each indicating a preclearing event, can be seen. After the clearing events conclude, a dark spot can be seen, indicating damage. To enhance visibility, the sample used for this video does not have an encapsulating layer atop the electrode closest to the camera.

Movie S2. Free displacement of a 6-layer hybrid-electrode rolled actuator driven at 1000V and 400Hz. Filmed at 20,000fps with a high-speed camera, Phantom V1612, the video is played back at 1/500× speed. A displacement of 0.9mm can be observed.

Movie S3. Free displacement of 100-layer actuator with diameter 1.5cm, and thickness 1cm. Filmed at 30 fps with a Nikon D7500 DSLR and played back at 1× speed. A voltage of 3100 V is applied at 1 Hz, and a through-thickness strain of 15% can be observed.

Supporting Information References